ARMY RESEARCH LABORATORY

# Visualization and Data Analysis Techniques for Ultra-Wideband Wide-Angle Synthetic Aperture Radar Data

Lam Nguyen

ARL-TR-1959 September 1999

The findings in this report are not to be construed as an official Department of the Army position unless so designated by other authorized documents.

Citation of manufacturer's or trade names does not constitute an official endorsement or approval of the use thereof.

Destroy this report when it is no longer needed. Do not return it to the originator.

**Army Research Laboratory**

Adelphi, MD 20783-1197

**ARL-TR-1959** **September 1999**

# Visualization and Data Analysis Techniques for Ultra-Wideband Wide-Angle Synthetic Aperture Radar Data

Lam Nguyen

Sensors and Electron Devices Directorate

## Abstract

The U.S. Army Research Laboratory (ARL) has designed, developed, and constructed an ultra-wideband synthetic aperture (UWB SAR) imaging radar to detect obscured targets, such as vehicles concealed by foliage and objects buried underground. As part of this effort, ARL has developed the software called UWBView to support the study of this imaging radar. The software can be employed in both field test and laboratory situations. In a field test, it provides a tool to perform certain signal processing tasks and to quickly assess radar data quality. In the research environment, it provides analysts with data visualization and analysis capabilities to support the phenomenological studies of targets and clutter. In a data processing environment, the software performs data and signal processing tasks. This report discusses the current software features and sample studies of UWB radar data using the software.

# Contents



## Figures

**Tables**

# 1. Introduction

The U.S. Army Research Laboratory (ARL) has designed, developed, and constructed an ultra-wideband synthetic aperture (UWB SAR) imaging radar to detect obscured targets, such as vehicles concealed by foliage and objects buried underground. A summary of this radar can be found in Ressler et al [1]. The radar is mounted atop a 150-ft telescoping boomlift to emulate the data collection geometry of a helicopter or unmanned aerial vehicle. This radar covers 20 to 1100 MHz and the full polarization matrix to accomplish this task. Extensive data collection efforts in support of both foliage-penetrating (FOPEN) and ground-penetrating (GPEN) objectives have resulted in massive amounts of collected data. Each pass from a data collection results in several gigabytes of raw radar data. During data collection, the radar's real-time signal processing algorithms perform data presumming to increase the signal-to-noise ratio (SNR), reduce radio-frequency interference (RFI), and reduce the data flow rate. Additional post-processing algorithms further process these data. The image formation process requires knowledge of the precise radar's location along the aperture; the radar motion compensation (MOCOMP) algorithm accomplishes this task. The UWB radar, with its wide bandwidth, makes it susceptible to strong interfering signals. Raw radar data have two interfering components that must be removed before the data can be used. The first component is self-interference, caused by local currents induced by the radar into the boom-lift support structure. The second component is strong RFI, such as local FM and TV broadcast signals. The self-interference removal (SIR) [2] and RFI extraction [3] algorithms perform the required signal processing tasks. Radar data are often filtered to a particular frequency band to emulate the operating region of a practical UWB radar and provide studies of tradeoff between frequency bands, detection performances, etc. The processed down-range data are then used to form SAR image. ARL has been employing the back-projection algorithm [4] for SAR imaging. The ultimate goal of ARL's effort is to evaluate the detection capability of a UWB radar. The produced SAR images are stored in a database for the development of automatic target detection (ATD) algorithms. Figure 1 illustrates the sequential data processing steps involved.

Although the collection of existing software for the aforementioned algorithms forms a powerful data and signal processing toolkit for the UWB radar, it lacks the important data visualization feature. It also has the following disadvantages: (1) Since the software programs require a specific computer platform and operating system (their advantage in

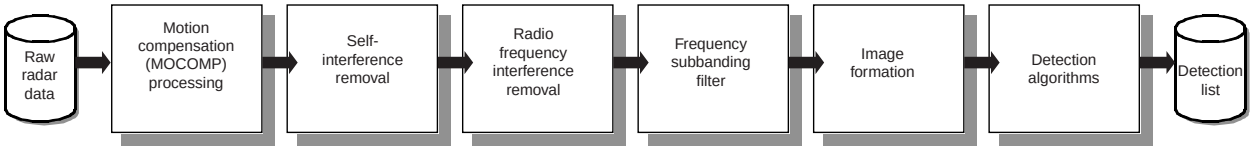


**Figure 1. Data processing steps.**

speed leads to disadvantages in usability, maintainability, and portability), they are incompatible with each other and new computer architecture. (2) Each software program exists in a different environment, with no intercommunication to others. (3) The programs lack a friendly graphical user interface (GUI). (4) None provides analysis or data visualization functions to give instantaneous feedback to analysts. An integrated software environment, called UWBView, is under development to satisfy these requirements: (a) compatibility that extends to multiple platforms and operating systems; (b) a friendly GUI; (c) data visualization and analysis functions to support a variety of data types, such as raw data and SAR images; and (d) integration of data and signal processing algorithms, including image formation.

The software can be employed in both field test and laboratory situations. In a field test, it provides us a tool to perform certain signal processing tasks and to quickly assess radar raw data, MOCOMP, and image quality. In the research environment, analysts can use this tool to study the phenomenological data associated with targets and clutter. In a data processing environment, the software performs data and signal processing tasks. With its GUI, analysts can quickly change signal processing parameters and visualize results. To date, many of the features have been implemented in this integrated environment. This report discusses the current software features, procedures to invoke them, and sample studies of UWB data using the software. Future work is also discussed.

# 2. UWB Data Analysis

## 2.1 Prefocus Data

### *2.1.1 Prefocus Data Description*

The radar is located atop a 150-ft telescoping boom lift and traverses along an aperture that is perpendicular to the imaged area. It transmits a burst of 128 pulses, with a pulse repetition frequency (prf) of 750 Hz (the transmit impulse has the bandwidth above 1 GHz), via the vertically polarized antenna. The two receive antennas (one with vertical polarization and the other with horizontal polarization) simultaneously receive the returned pulses to produce two channels of incoming signals. The radar then switches to the horizontally polarized antenna to transmit another burst of 128 pulses. The two receiving antennas then produce another pair of received signals. Thus, at each position, a complete set of polarization signals is produced: VV, VH, HV, HH. The first and second letters represent the polarizations of the transmit and receive antennas, respectively. (V stands for vertical and H stands for horizontal.) Incoming signals from the two channels are digitized simultaneously at the rate of 2 Gsamples/s and then transferred to the computer system for signal processing.

Each burst of 128 data records is transferred to a buffer in a digital signal processor for processing, where the records are coherently interleaved to an equivalent of 64 Gsamples/s. The resulting interleaved record is then time-shifted according to channel delay, low-pass filtered at 1.5 GHz, and decimated to an 8 Gsamples/s rate. Since two channels are operated simultaneously and data flow into the computer system in real time, multiple signal processors are needed to sustain the high input data rate. When a processor finishes its signal processing task, data are sent to the host computer to be archived in storage devices. The antenna's position information is recorded by the MOCOMP subsystem. These radars' MOCOMP information is also embedded in the data stream to be recorded in the storage devices [5].

When a data collection pass is completed, the radar data and MOCOMP information are brought back into the laboratory for further processing. The MOCOMP processing algorithm estimates the antenna's location for each down-range record (the MOCOMP information is recorded at a much slower rate than the radar measurement). When the MOCOMP information is transmitted from the geodimeter to the radar for recording, there is a time delay introduced by this communication. This MOCOMP latency is also corrected at the MOCOMP processing stage. The down-range data are then processed to remove SIR and RFI, and may be filtered to a particular frequency subband. The resulting data are used as the raw "phase history" data. When this step is completed, four different PFDs are generated, which correspond to the four polarization configurations. The PFD file follows the Tagged Interchange File Format (TIFF 6.0) specification [6], an industry standard created by the Aldus Corporation for

storing images. Each TIFF file contains a number of tags that specify what information is included and where they are located in the file. The PFD file follows the TIFF specification, except that we define our own tags to include radar and other information. Table 1 lists the contents of the PFD file and the corresponding tags. Note that radar data are converted from a 32-bit floating-point format to a 16-bit integer format before they are saved in a PFD file for storage efficiency. Thus, when data are read from a PFD file, they should be properly scaled with scaling information from the PFD file. Another point worth noting is that the PFD file is generated using the big-endian format. Since the software should be platform-independent, it must detect the CPU type (big-endian or little-endian) at run time to handle the data properly.

### 2.1.2 *PFD Data Analysis*

Figure 2 (see p. 6) shows the File pop-up menu. Currently, the software supports several file types. To access a PFD file, one selects Open PFD File. The file selection window lets users either enter the file name or browse through the file system to select the PFD file. After the PFD file is entered or selected, the Selection Coordinate Window (see fig. 3 on p. 6) prompts the user to choose the coordinate system. During data collection, MOCOMP information is recorded with the Universal Transverse Mercator (UTM) coordinate system. However, for analysis, the MOCOMP information should be converted to the radar coordinate system (in which the $x$ component is along track, and the $y$ component is down range). If coordinate conversion is not required (the MOCOMP is already in the radar coordinate system), users can select the option None in the selection window. Figure 4 (see p. 6) illustrates the typical data collection geometry. The radar is set at a height of about 45 m and traverses along an aperture of 2 km.

After the PFD file is selected, all the visualization and analysis functions related to PFD are ready to be invoked. To view the information related to the PFD file, click PFD File Information under the PFDView menu. The PFD File Info window will pop up, displaying the information associated with the file (see fig. 5 on p. 7).

#### 2.1.2.1 *Radar MOCOMP*

To view the information associated with radar data along the aperture, such as MOCOMP information, data acquisition timing, attenuation, and position index, users select PFD Header Plot under the PFD View menu. The pop-up PFD Header View window (see fig. 6 on p. 7) displays the plot area, the data type selection menu, and the sliders to control the starting and ending aperture index of the plot. The following information can be viewed:

*MOCOMP information*.—The three coordinates, $x$, $y$, and $z$, can be examined. Depending on the coordinate system selected when the PFD file is opened, the MOCOMP information can be in either UTM or radar coordinate system. Figure 7 illustrates an example where the same PFD file as in figure 4 is accessed, except that the UTM coordinate system is selected.

**Table 1. PFD file format.**

| Tag | Name | Description | Data type | Number of elements |
|---|---|---|---|---|
| 65116 | NUM_APERTURES | Number of aperture positions (also the number of raw radar records) | 16-bit integer | 1 |
| 65119 | SAMPPREIOD | Data sampling period in seconds | Float | 1 |
| 65120 | DATARECLENGTH | Number of samples per data record | 31-bit integer | 1 |
| 65101 | DATAFILE_TIMESTAMP | Date of run | ASCII string with format: mm/dd/yy | 8 |
| 65106 | RUN_DESCRIPTION | Description for run | ASCII string | Varied |
| 65107 | PASS_NUMBER | Unique run identification | 32-bit integer | 1 |
| 65114 | RUN_STARTPOSITION | Aperture position index for first record | 32-bit integer | 1 |
| 65115 | RUN_ENDPOSITION | Aperture position index for last record | 32-bit integer | 1 |
| 65127 | MOCOMP_UTME | MOCOMP information: UTM east (in meters) | Float | NUM_APERTURES |
| 65126 | MOCOMP_UTMN | MOCOMP information: UTM north (in meters) | Float | NUM_APERTURES |
| 65128 | MOCOM_UTMH | MOCOMP information: UTM height (in meters) | Float | NUM_APERTURES |
| 65132 | MOCOMP_ACQTIME | Time between transmit pulse and first sample of received signal | Float | NUM_APERTURES |
| 65125 | MOCOMP_POSITION | Aperture position index | 32-bit integer | NUM_APERTURES |
| 65134 | SCALE_X | Scaling factor (transmit) to be applied to data record | Float | NUM_APERTURES |
| 65135 | SCALE_R | Scaling factor (receive) to be applied to data record | Float | NUM_APERTURES |
| 65136 | MOCOM_ATTEN | Attenuation setting (in decibels) | Float | NUM_APERTURES |
| 65111 | XMIT_POLARIZATION | Transmit polarization: horizontal or vertical | ASCII | Varied |
| 65112 | RECV_POLARIZATION | Receive polarization: horizontal or vertical | ASCII | Varied |
| 65145 | CAL_SCALE | Scaling factor (calibration) to be applied to data record | Float | 1 |

*UTM = Universal Transverse Mercator coordinate system.*

**Figure 2. Menu button to open PFD file.**

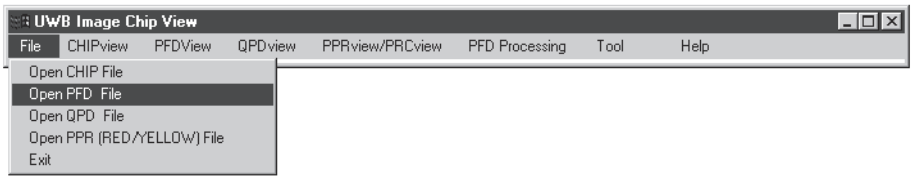


**Figure 3. Coordinate system selection menu.**

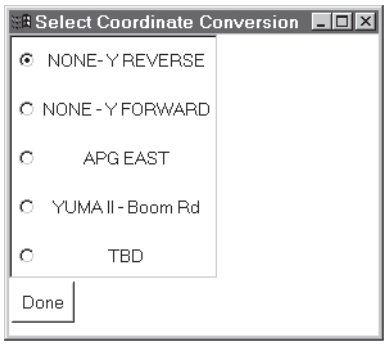


**Figure 4. MOCOMP data show typical data collection geometry.**

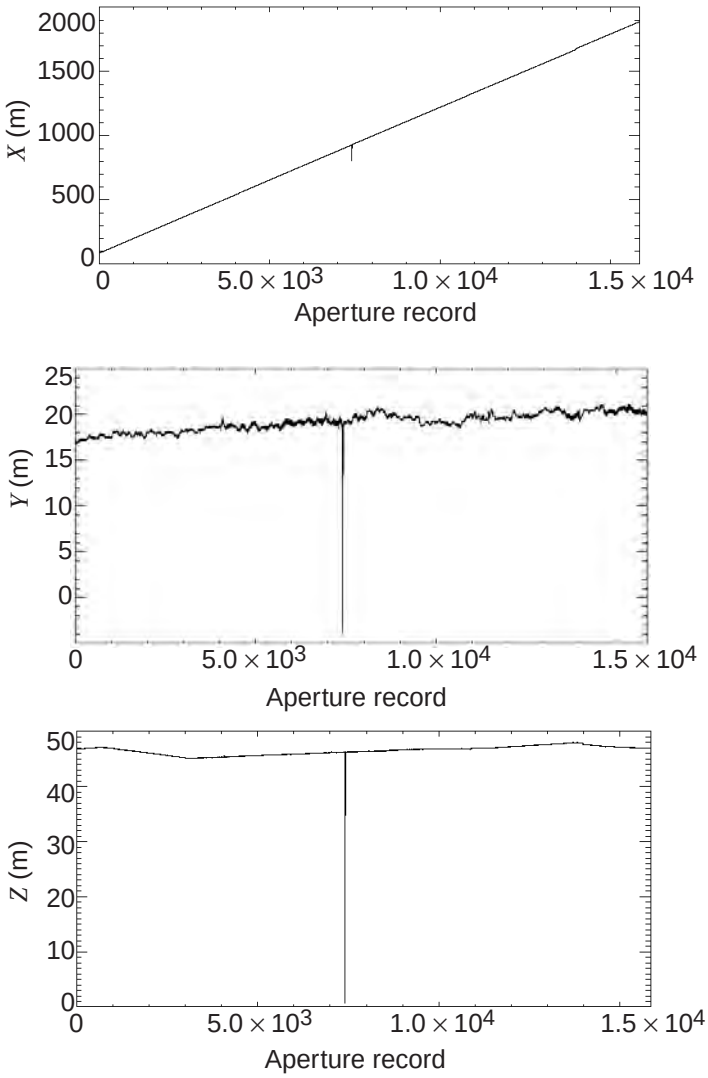

Although the information in figures 6 and 7 is equivalent, it is much easier to visualize the radar motion with the radar coordinate system shown in figure 4, where the $x$- and $y$-components show the radar motion in the along-track and the down-range directions, respectively. Note that in the radar coordinate system the $x$-component increases linearly as the radar moves away from the reference point, where the geodimeter is located, while the $y$-component is almost constant across the aperture.

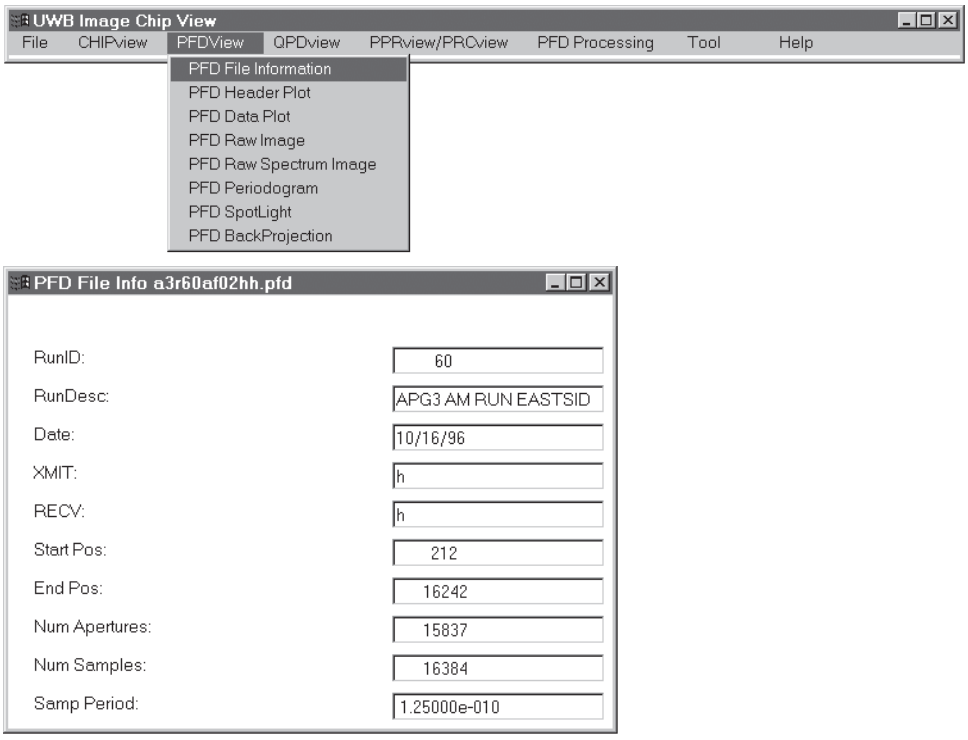


**Figure 5. Viewing PFD file information.**

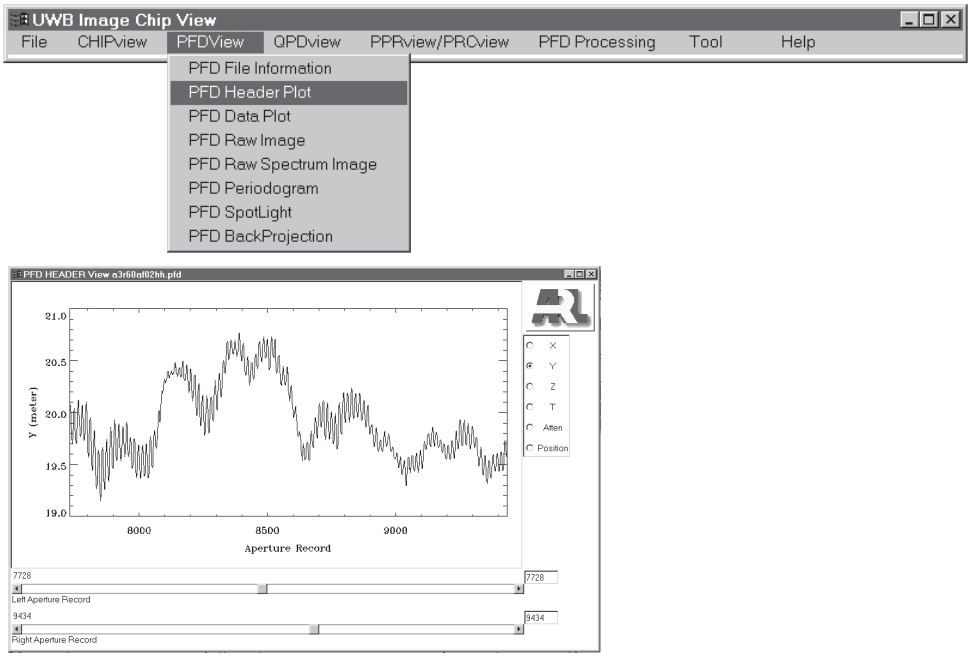


**Figure 6. Viewing PFD header information. In this example, *y* component of MOCOMP is selected.**

**Figure 7. Same MOCOMP data as in figure 4, except UTM coordinated is selected.**

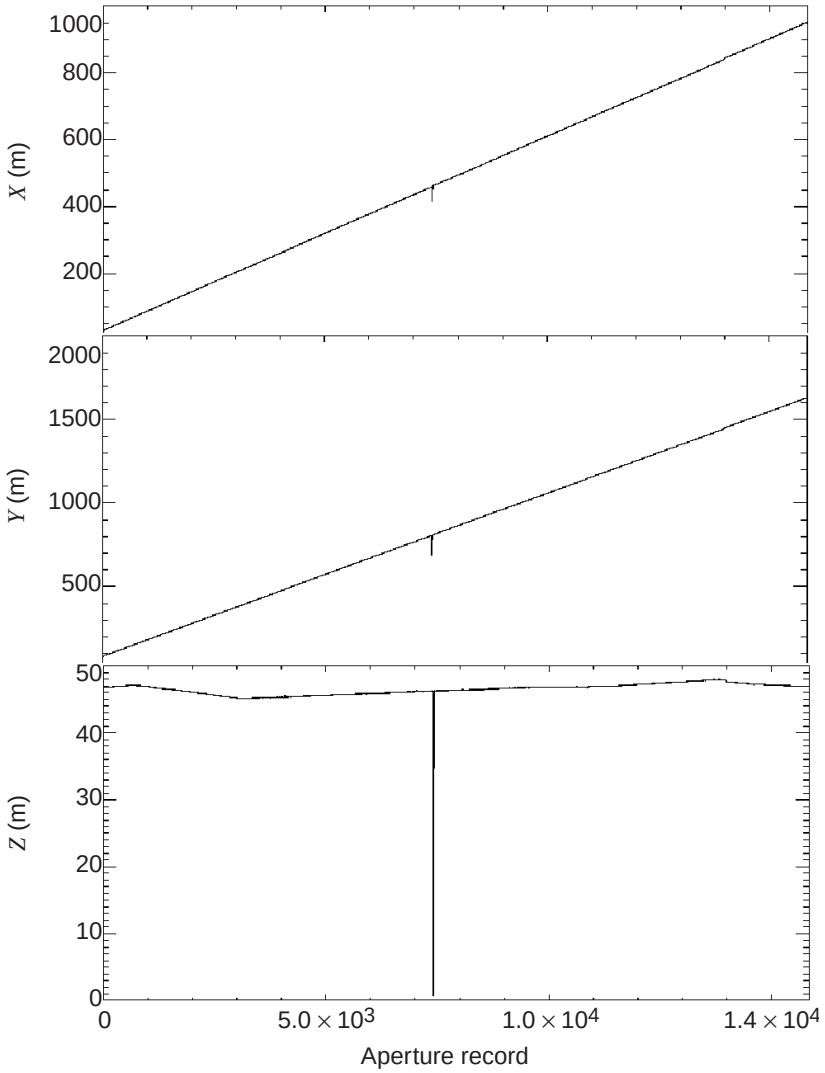


Any variation in the *y*-component reflects the change in distance from the radar to the image area. Figure 6 shows the zoomed-in view of the *y*-component. The slow variation in the plot is due to the motion of the crane, while the oscillatory component results from the vibration of the boom and basket (that holds the antennas and the radar system) during motion.

*Data acquisition timing*.— This is the delay between transmission of the pulse and the first digitized sample of the received signal. It is used to set the radar standoff range. The system delay timing, due to cables, is compensated by the radar real-time signal interleaving algorithm. However, some error is introduced into this acquisition delay timing by the antenna phase centers and other components. The focused image is based on the coherent integration of radar data across the aperture. Therefore, the precision of the data acquisition timing (and also the MOCOMP information) is extremely important to the quality of the focused image. The data acquisition timing is usually adjusted according to a particular radar configuration. Although the delay acquisition timing can be varied with aperture position, we keep it constant in a typical configuration.

*Attenuation setting*.—The radar has a software-based automatic gain control (AGC) system. Although we do not need this information to process data (the data scaling factor is included in SCALE_X, SCALE_R, and CAL_SCALE in table 1), it is useful to verify the proper operation of the radar. Figure 8 shows an example of the attenuation setting across the aperture. Note that at some sections of the apertures, the attenuation goes up to 16 dB. This is caused by the strong returned signal from the radar test targets (8-ft trihedral), which can be verified easily by viewing data at the corresponding sections of aperture.

*Position information*.—Every radar down-range record across the aperture is assigned a position index. However, not all the records are saved into the PFD file. Some of them are RFI sniff records (this is measured every 250 positions). Others are invalid data records caused by problems in the data acquisition subsystem or MOCOMP subsystem. Data and position information are saved together in the PFD file; thus, the record index in the PFD file is not the same as the position index. In some experiments (especially radar calibration), this position information is very important to keep track of what kind of data were measured in a particular section of the aperture.

### 2.1.2.2 *Data View*

Users select the menu button PFD Data Plot to access this feature. The PFD Data View window has a plot area, the data statistics area, data header window, and three sliders (see fig. 9). The plot area contains the data and its spectral plots. The statistics area shows the maximum, minimum, mean, and standard deviations from the zoom-in segment of data. The data header window shows all header information associated with this data record: MOCOMP $x$, $y$, $z$, data acquisition delay, attenuation, and position index. The first and second sliders are used to control the starting

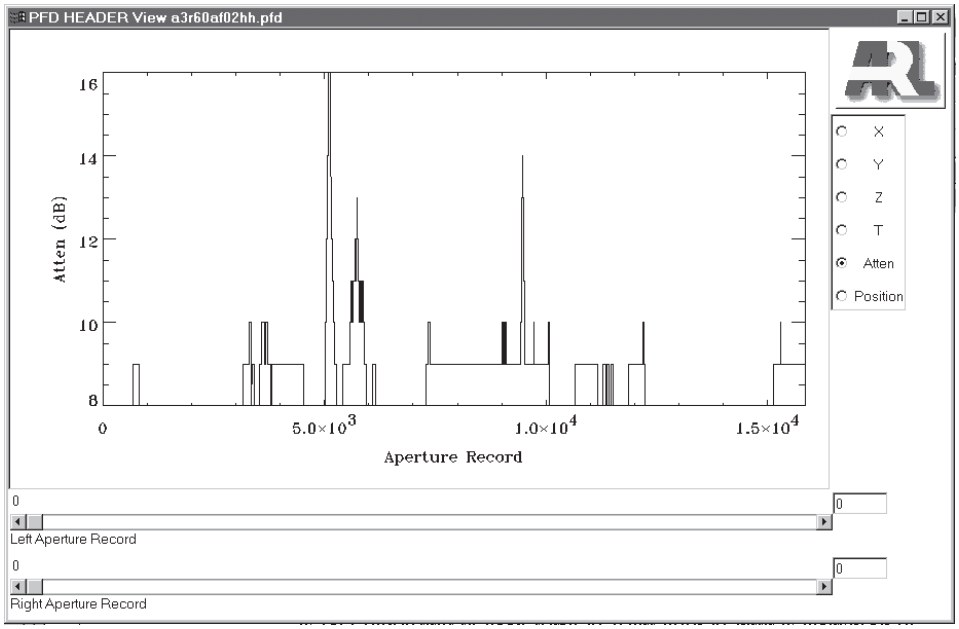


**Figure 8. Typical radar AGC attenuation information.**

**Figure 9. PFD data view window.**

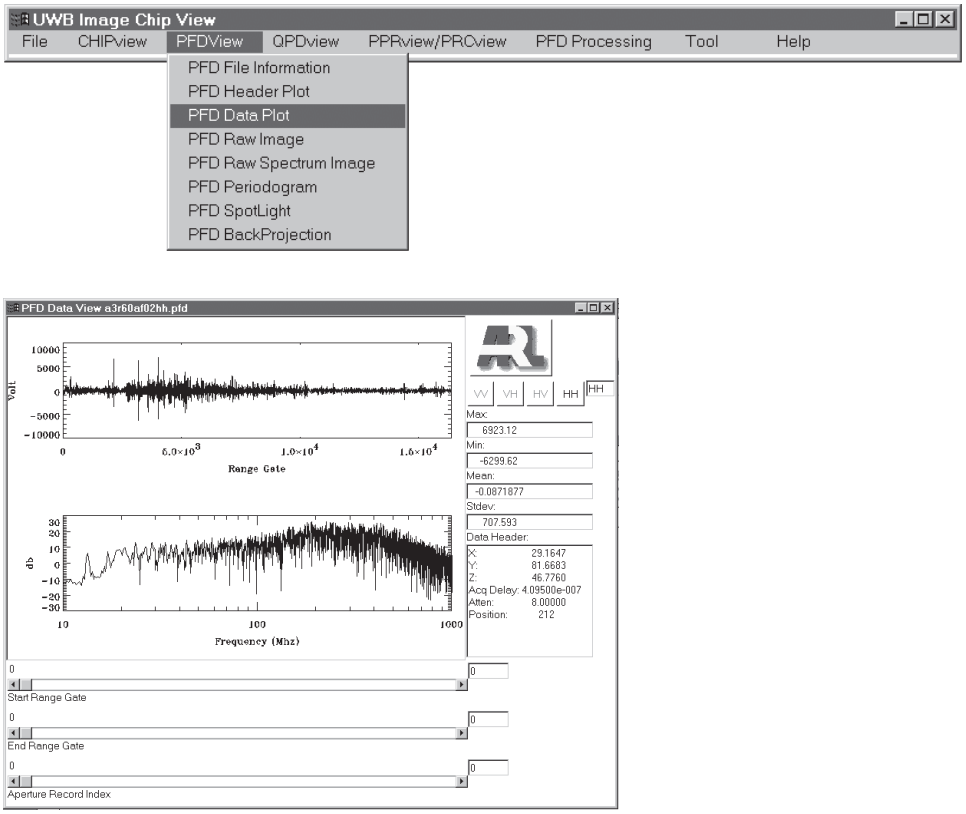


and ending range gates of the data segment to be viewed. The third slider is used to randomly access any data record in the PFD file. Each time the data plot is changed by using either the zoom-in sliders or the record selection slider, the spectral content of the data segment, its statistics values, and header display are all updated accordingly.

Figure 10 shows an example of a radar down-range record archived by the real-time system. The low-frequency component due to the SIR signal caused by the radar can be seen in both the time-domain data record and its spectrum. Figure 11 shows the same data record that has been processed by the SIR algorithm (see fig. 1 for processing sequence). The low-frequency component of the signal is removed, and targets can be recognized in the record. In figure 12, the RFI level in the record has been reduced by the RFI algorithm.

### *2.1.2.3 Raw Image View*

Raw radar data can also be viewed under a different perspective in the PFD Raw Image window. Figure 13 shows the menu button used to invoke this window, where we can view a group of data records as an image using colors to encode the amplitude. The color mapping is encoded so that both the positive and negative sides of bipolar signal can be visualized. The total dynamic range of the displayed image is 20 dB. The maximum value is mapped to the maximum color index (255), and any value that is 20 dB below the peak is truncated to the minimum color index (0). Thus, for a bipolar signal with equal amplitudes in both

**Figure 10. Raw radar range-compressed data and their spectrum.**

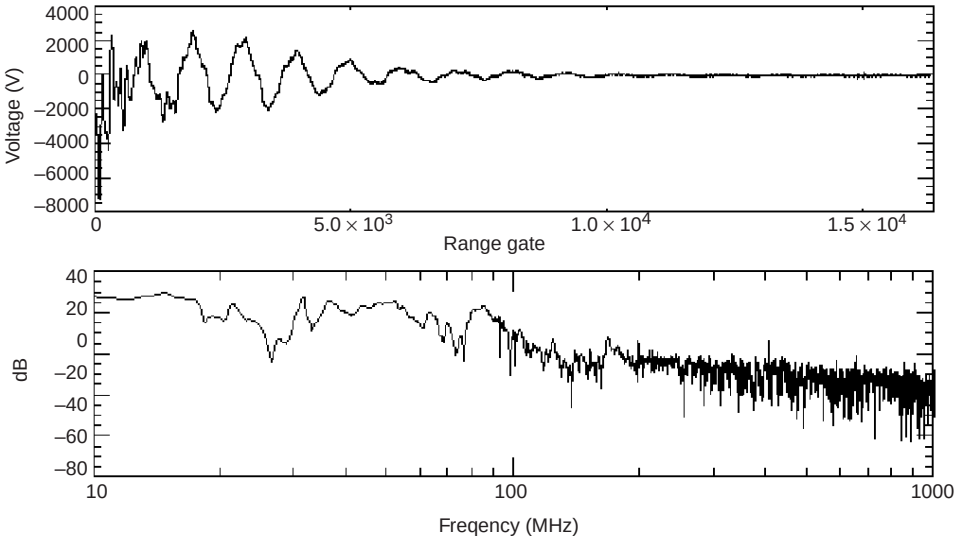


**Figure 11. Radar data after SIR is applied. Self-interference component is removed from record.**

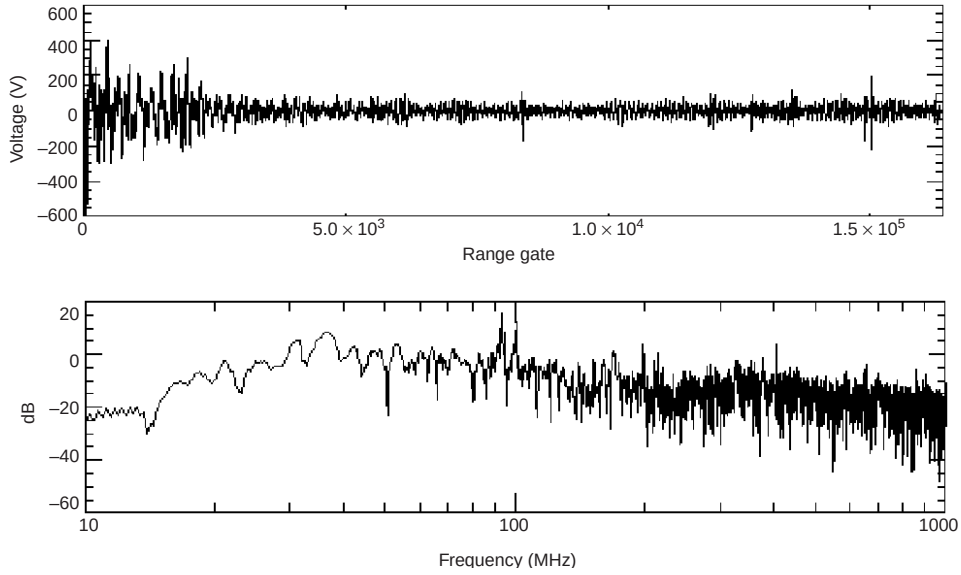


**Figure 12. Radar data after RFI is applied. Note that RFI level is reduced compared to that of figure 11.**

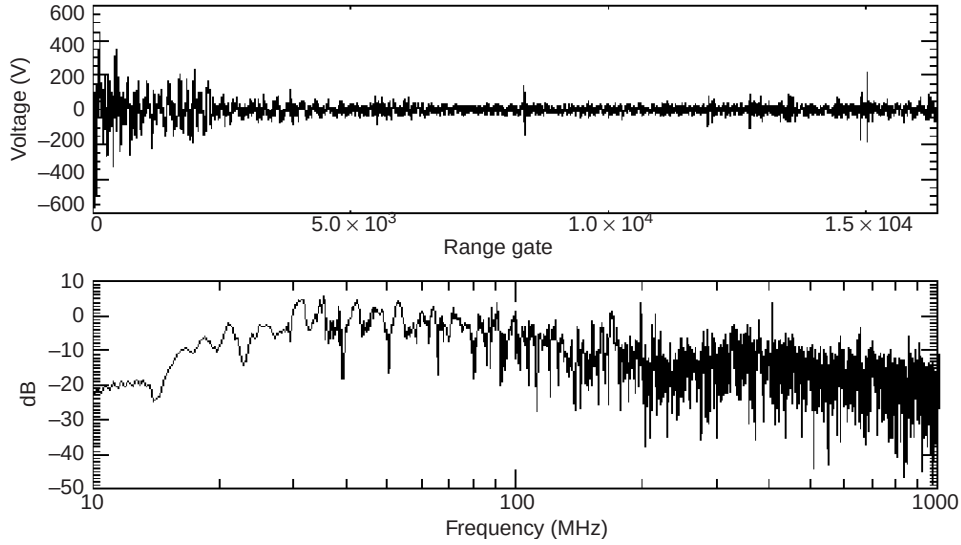

positive and negative directions, the transition from positive to negative value occurs at –6 dB from the peak.

Figure 14 shows the backscatter signals from a group of targets as the radar passes by. Each target forms a different parabola, whose trajectory depends on the geometry between the radar and itself. It is interesting to note that the responses from the telephone wire and its multi-path return signal are parallel with the along-track direction, while the response from each telephone pole forms a different parabola.

Figure 15 is an example in which the radar passes an 8-ft trihedral. It shows that the response from the trihedral changes with the aspect angle. Note that the motion of the boom lift has caused the trihedral parabola trajectory to be modulated by a small amplitude sine wave (see fig. 6).

**Figure 13. Raw image menu.**

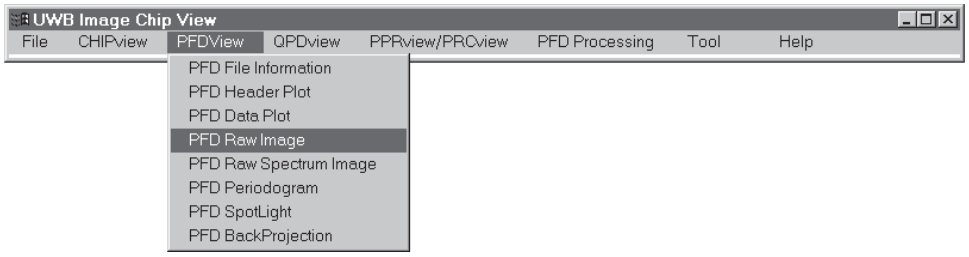


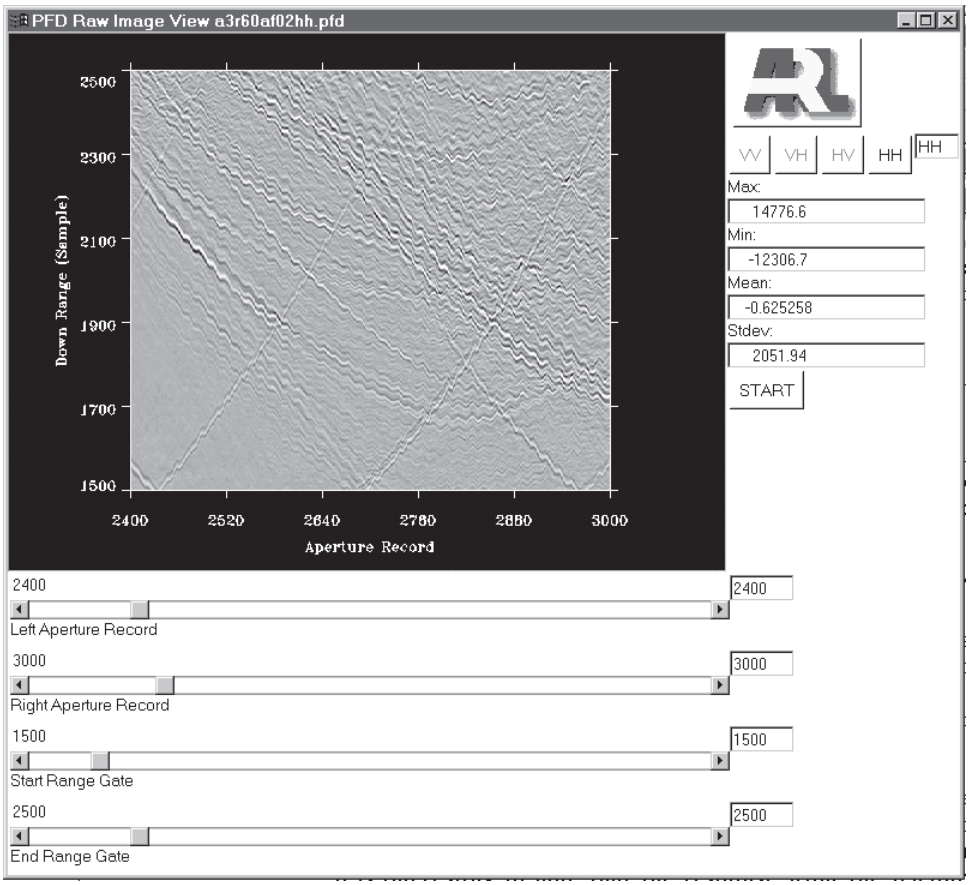

**Figure 14. Example of raw image view.**

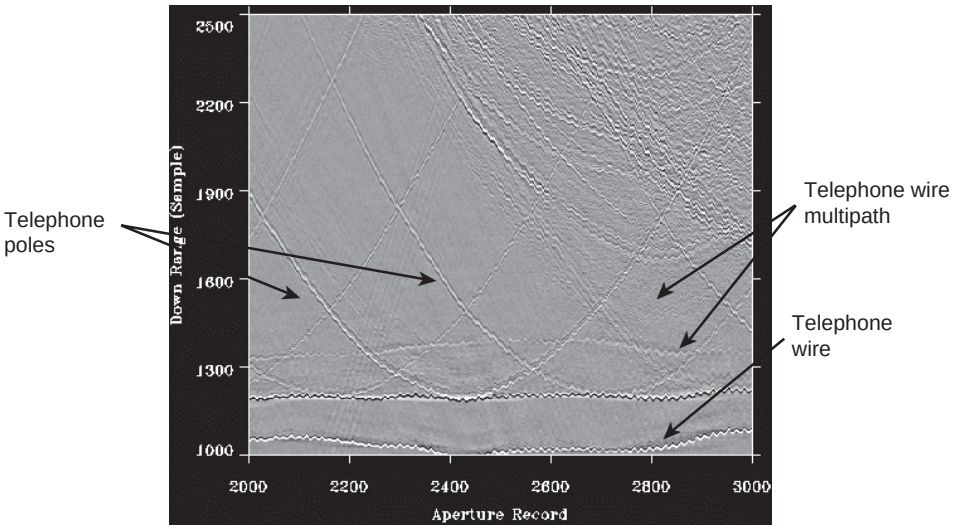


**Figure 15. Raw image of 8-ft trihedral.**

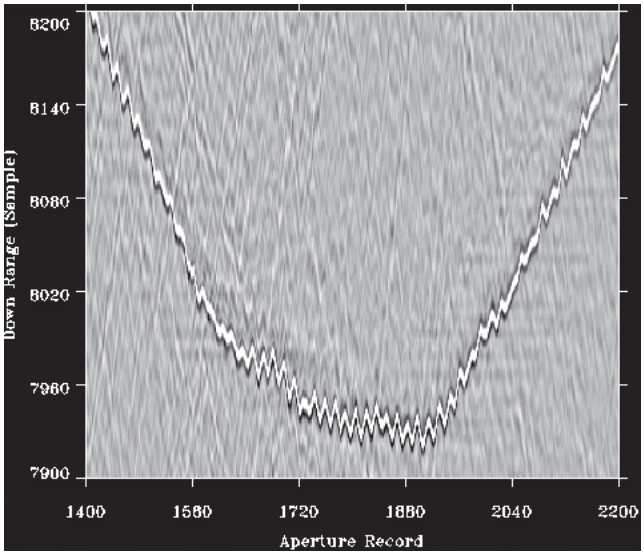


Also, its response did not form a symmetrical parabola, since the radar path was not a straight line.

Figure 16 is another example of how this visualization can detail the backscattering properties of a target. It shows the returned signal from a semi-trailer positioned parallel to the radar path. There is a dominant return from the dihedral formed by the vehicle's wall and the ground that only occurs for a short aperture (nonisotropic target). Another backscatter component is the diffraction from the top edge of the vehicle, which shows as a weaker response before the dihedral return. As the radar is moving away from the vehicle, we can see a weaker but more complicated structure of the return signal.

Figure 17 shows how this visualization can be used to discover the radar's anomaly or an external source that causes artifacts to the data.

**Figure 16. Raw image of vehicle.**

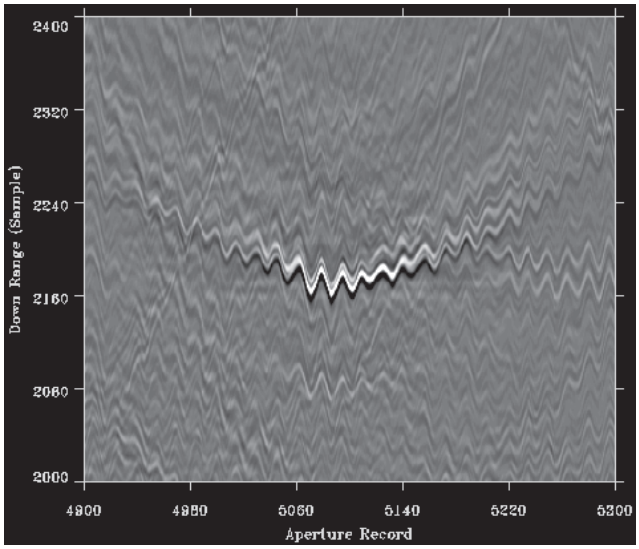


**Figure 17. Raw image that shows that radar has problem with transmitter.**

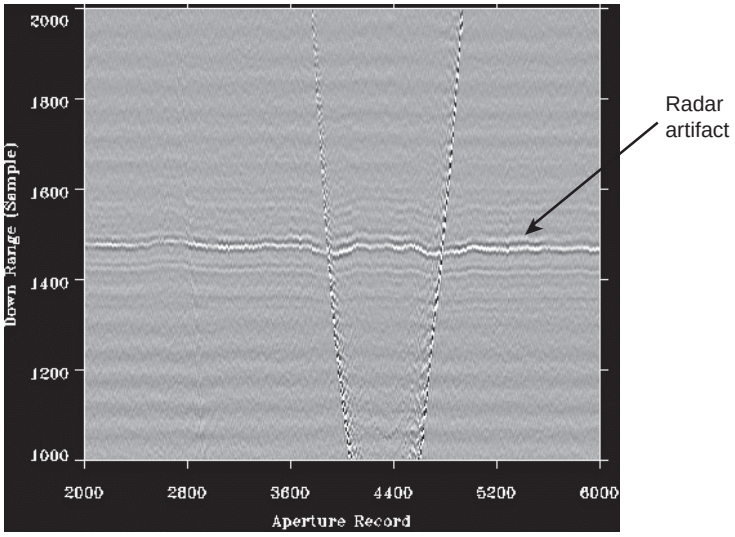


Besides the expected response from a target shown by its parabola, the image also shows a horizontal line, high-frequency signal that starts at about the same range gate across the aperture. This artifact results from a bad transmitter that causes spurious transmit pulses.

### *2.1.2.4 Periodogram*

Another useful analysis tool is the periodogram. Figure 18 shows the menu selection to access the periodogram window. In this analysis, we want to look at the spectral contents of the overall background. The spectral contents of any particular range line represent targets seen by the radar at that aperture position. However, the average of the spectral contents across a large aperture will decorrelate individual targets and be a good representation of the overall system response from the background. The spectral contents also show the RFI components that are consistent across the aperture. Figure 19 shows the periodograms for two different data collections at Aberdeen Proving Ground, Maryland. The

**Figure 18.**
**Periodogram menu.**

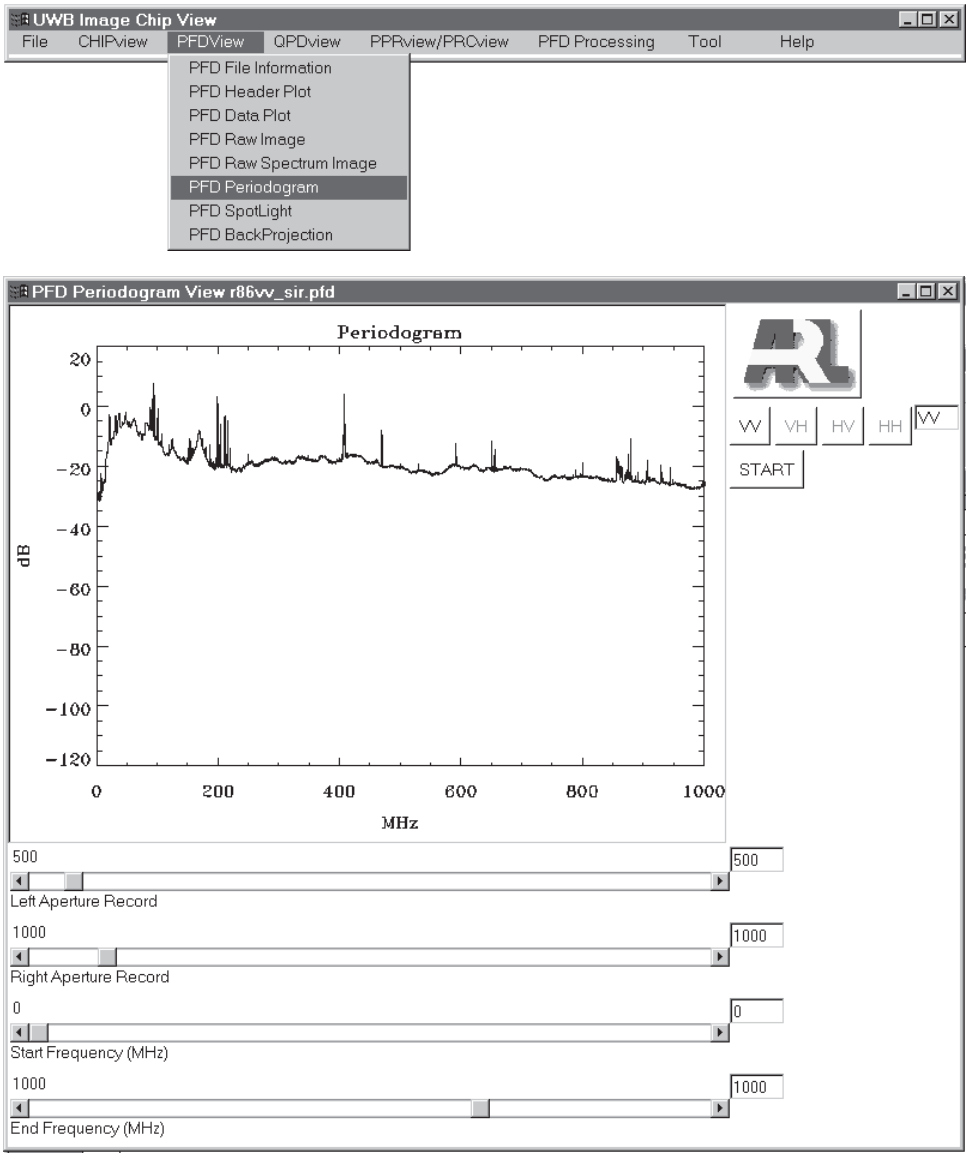


two plots show the periodograms from the (a) 50 to 1200 MHz and (b) 20 to 1200 MHz antenna sets. Although the two periodograms are generated from the same aperture section, they show different characteristics that well represent the two antenna sets employed. Note that the first periodogram (fig. 19a) shows a fairly flat spectral response across the frequency band. Figure 19b shows a much higher gain, particularly in the 150 to 500 MHz frequency band, and rolls off quickly at the higher frequency band. Four sliders are used to control the periodogram computation. The first set of sliders is used to set the starting and ending aperture positions. The second set of sliders is used to control the range of frequency for viewing the spectral content. After parameters are set, pressing the Start button will invoke the algorithm.

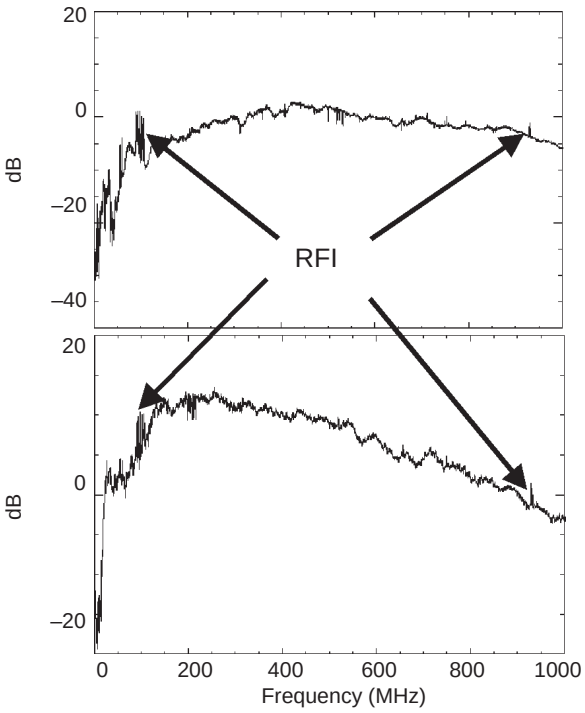


**Figure 19. Comparison of periodograms from (a) 50 to 1200 MHz and (b) 20 to 1200 MHz antenna set data.**

### 2.1.2.5 *Raw Spectrum Image*

This visualization tool allows us to view the spectral contents of radar data along a section of aperture. The spectral data are viewed as an image, where colors are used to encode its amplitude. Figure 20 shows the menu option to access the Raw Spectrum Image window. Two sliders are used to control the aperture section, and two others control the frequency range for viewing the spectral contents. The figure displays the spectral contents from 0 to 100 MHz of 100 records. Note that there are strong FM components in the 90 to 100 MHz band.

### 2.1.2.6 *Filtering Radar Data*

Radar data are often filtered to a particular frequency band to emulate the operating region of a practical UWB radar, to study the tradeoff between frequency bands and detection performances, or to remove interference from a particular band. Users can invoke the PFD Filter window (see fig. 21) by selecting the Filter pull-down button from PFD Processing Menu button. The user must fill in the required parameters: input, filter coefficient, and output filenames. The filenames can be typed in or selected using the built-in file selection menu. Users press the appropriate button (Browse Input File, Browse Filter File, or Browse Output File) to navigate through the file system and select the corresponding file. The data format of the filter file should be as follows: The first word is a 32-bit-long integer that represents the number of taps in the filter. This should be an odd number to yield a zero-phase shift in the output data. Following this word is the floating-point array of filter taps. The filter data should be stored using the big-endian format to be consistent with other data.

**Figure 20. Raw spectrum as image.**

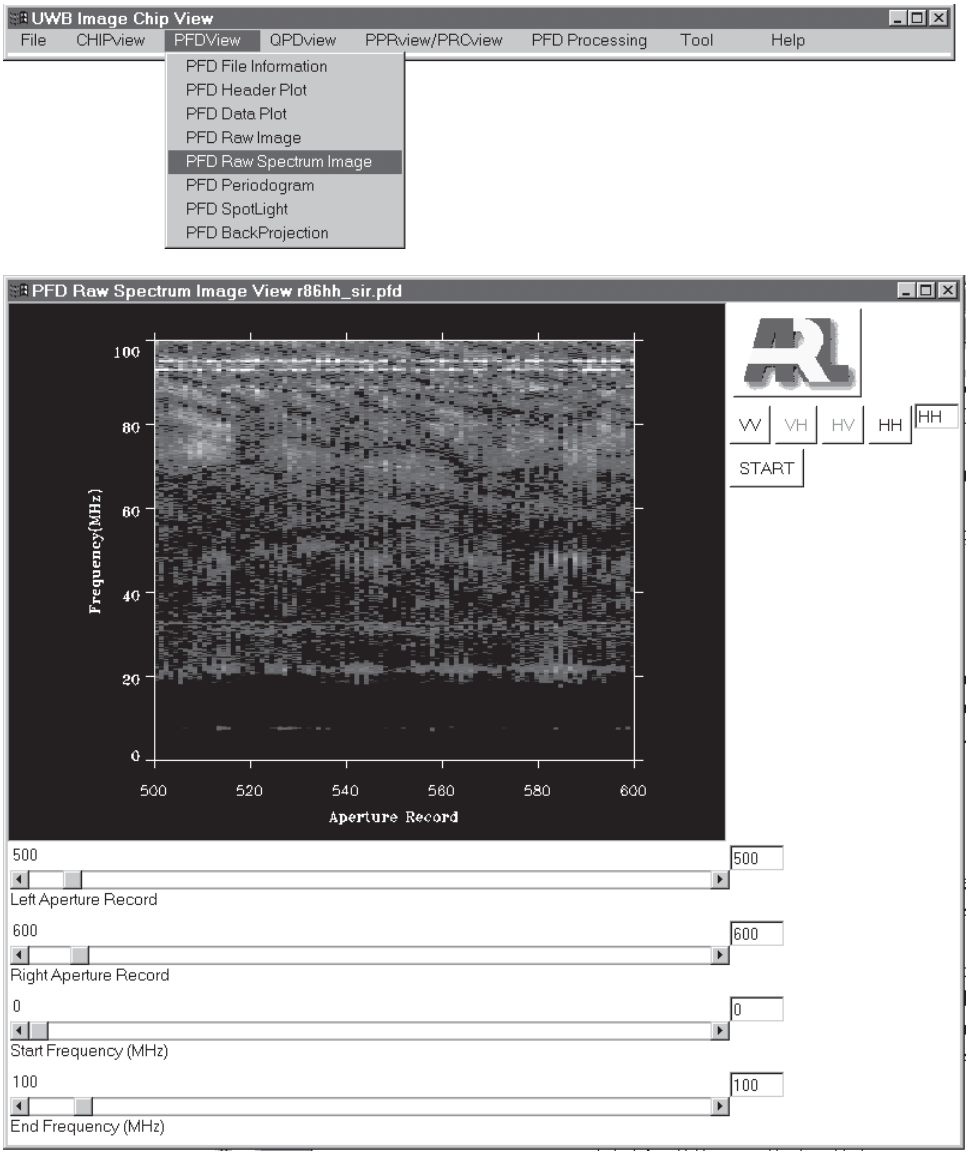


**Figure 21. Filter menu.**

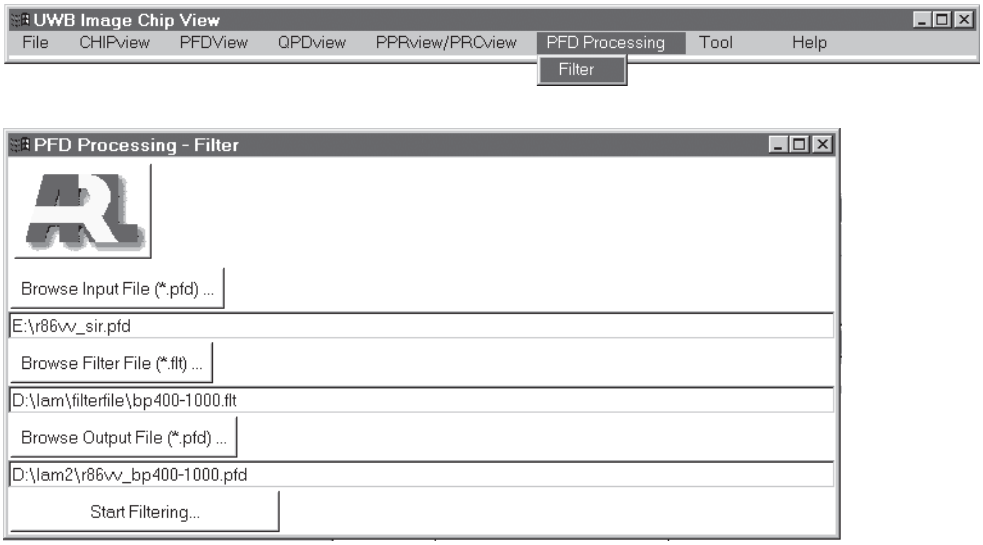

#### 2.1.2.7 *UWB SAR Image Formation*

ARL has employed the backprojection (delay-and-sum beamformer) technique to form UWB SAR images [4]. The process, in which all data across the aperture are coherently summed, produces SAR images with high resolution in both the down-range and cross-range directions, high SNR, and wide frequency bandwidth. Consider a radar that moves along a synthetic aperture with $N$ positions, facing an area to be imaged. At position $k$ in the aperture, the antenna phase center has the coordinates ($xr_k$, $yr_k$, $zr_k$). The returned down-range signal at position $k$ is $s_k(n)$. Consider a pixel at $i$th range bin and $j$th cross-range bin in the image grid. It has the coordinates ($xp_{i,j}$, $yp_{i,j}$, $zp_{i,j}$). The value of the pixel at the output of the focuser will be the coherent integration of all the values contributed to that pixel along the aperture. The pixel value is computed as

$$P_{i,j} = \sum_{k=0}^{N-1} w_k \, s_k(f(i,j,k)) \ , \tag{1}$$

where $f(i, j, k)$ is the shift index to the signal $s_k$, and $w_k$ is the weight at $k$th aperture position. Thus, the process is to find the shift index for every pixel at every position in the aperture.

In order to calculate the function $f(i, j, k)$ for the shift index, we need to calculate the distance between the antenna and the pixel at any position, which is

$$R_{i,j,k} = \sqrt{\left(xr_k - xp_{i,j}\right)^2 + \left(yr_k - yp_{i,j}\right)^2 + \left(zr_k - zp_{i,j}\right)^2} \ . \tag{2}$$

The corresponding round-trip time between the antenna phase center and the pixel is

$$t_{i,j,k} = 2\,\frac{R_{i,j,k}}{c} \ , \tag{3}$$

where $c$ is the speed of light.

Thus, the shift index $f(i, j, k)$ is

$$f(i,j,k) = \frac{t_{i,j,k} - t_{Acq}}{t_s} \ , \tag{4}$$

where $t_{Acq}$ is the acquisition delay timing (the time between the pulse is transmitted and the returned signal digitized), and $t_s$ is the sampling period of the down-range signal. Since the signal $s_k$ is discrete, the index $f(i, j, k)$ should be rounded off to its nearest integer. This approach is acceptable if the sampling rate of $s_k$ is higher than that of the image. Otherwise, $s_k$ should be upsampled before performing backprojection.

Figure 22 shows how to invoke the backprojection main window. The following parameters are required for image formation.

**Figure 22. Image formation menu.**

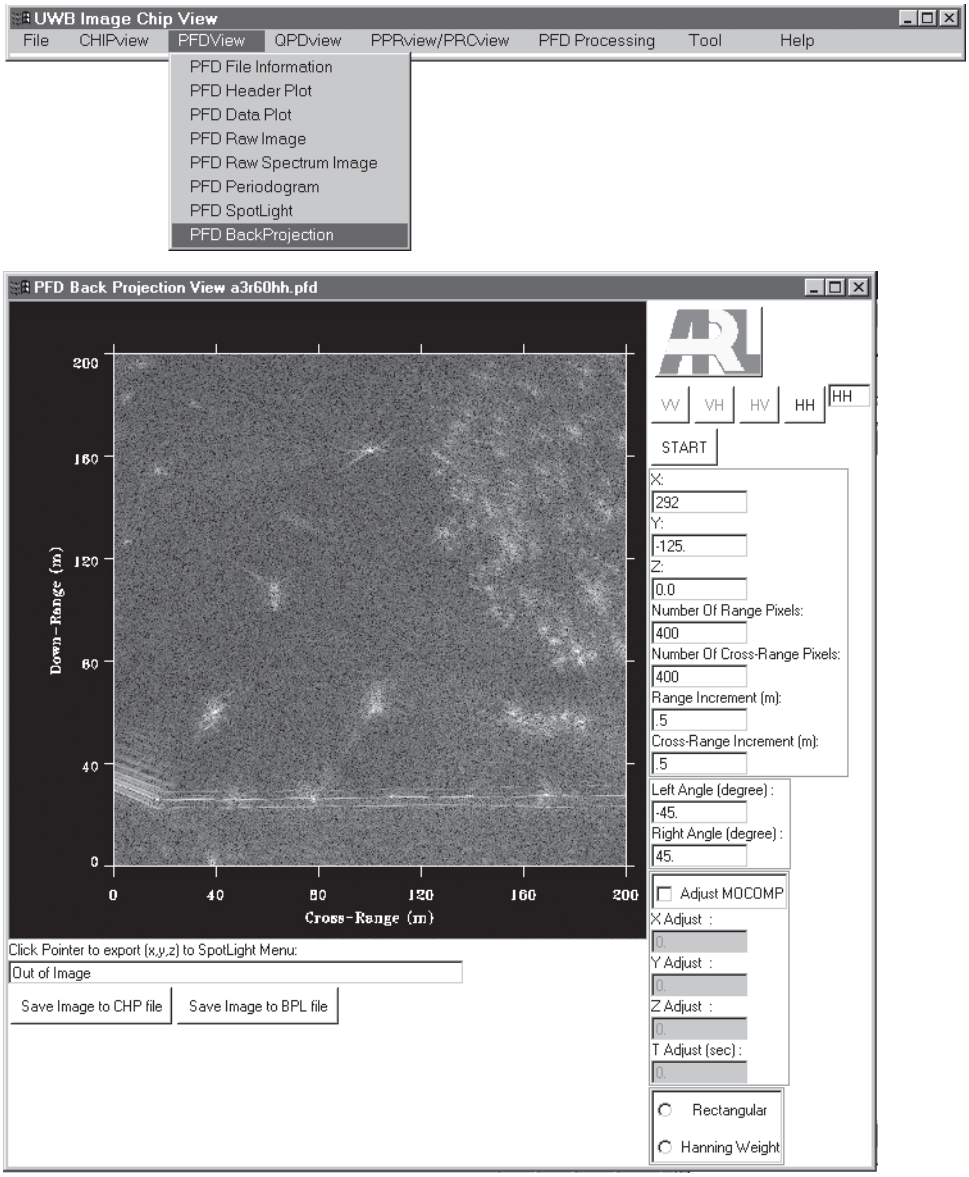


*Image center*.—The image center, together with the number of pixels and pixel spacing, completely defines the imaging area. In a typical radar setting, the radar height is 45 m, the standoff range is 64 m (the acquisition delay time is 430 ns), and the range swath is 300 m (each data record has 16,384 samples at 8 GHz sampling rate). This radar setting translates to the image center at about 195 m from the radar in down-range direction. The image center can be changed to form an image at any area of interest. Note that the down-range direction (direction of *y*-axis) is important to determine the image center. In most cases, the geometry is set up to have the radar down-range direction pointing to the negative *y*-axis. That means a pixel would have a more negative *y*-value as it moves away from the radar. In theory, if an aperture is a perfect line, both images focused in the front and the back of the aperture are identical. However, the radar path is not a straight line in reality. Thus, if the sign of the *y*-direction is not correctly specified, the formed image is actually located

in the back of the aperture, resulting in a defocused image. Figure 23 shows an example where both the image areas in the front and back of the aperture are formed.

*Number of pixels*.—The user can specify the number of pixels in both the down-range and cross-range directions.

*Image gridding*.—This specifies the spacing in both down-range and cross-range directions. The typical setting is 3.75 cm in down-range (equivalent to 4 GHz sampling rate) and 11.25 cm in cross-range. A user can change these settings using the Range Increment and Cross-Range Increment input textboxes. For a quick look at a large image area, the image gridding should be set using coarse values, for example, 0.5 m. After the image is formed, the user can form an image from an area of interest using higher resolution.

*Aperture integration angle*.—The left and right angle input parameters are used to control the section of aperture used to form the image. Figures 24 and 25 show the importance of the integration angle in image formation and target/clutter discrimination.

The high resolution in cross-range of SAR images is achieved by integration across a long aperture. To keep the cross-range resolution nearly constant throughout the image, ARL has been using a mosaic technique, which divides a large image grid into small tiles. Data are backprojected into each tile using an aperture with an integration angle of 90° ± 4.5°. Figure 24 shows that the cross-range resolution of an 8-ft trihedral increases with respect to integration angle.

Anisotropy (nonuniform backscatter as a function of look angle) plays an important role in discriminating a target from clutter [7]. Using multiple subapertures to form an image, flashes from vehicles might be detected. On the other hand, tree clutter might have more uniform backscattering across the aperture. Figure 25 shows images of a vehicle that are formed using data from three mutually exclusive, 30° subapertures—one from broadside and two from left- and right-squinted beams. A user can control the squint, as well as the total integration angle, by entering the appropriate settings in the Left Angle and Right Angle input textboxes.

**Figure 23. Image areas in front and back of aperture are formed.**

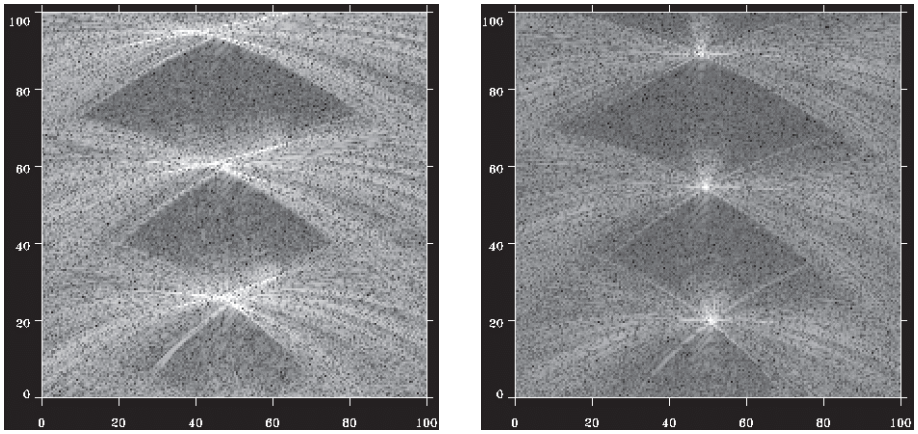

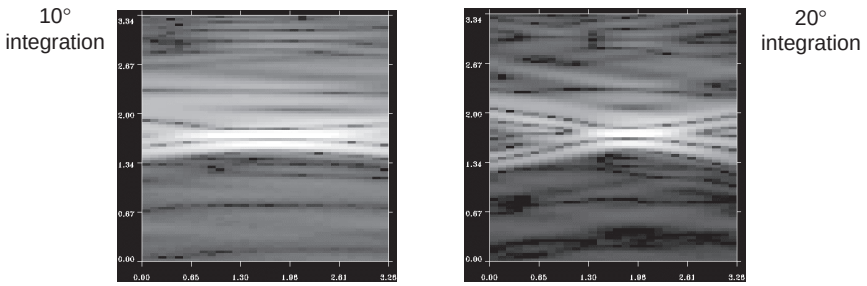


**Figure 24. Crossrange resolution of 8-ft trihedral increases as integration angle increases.**

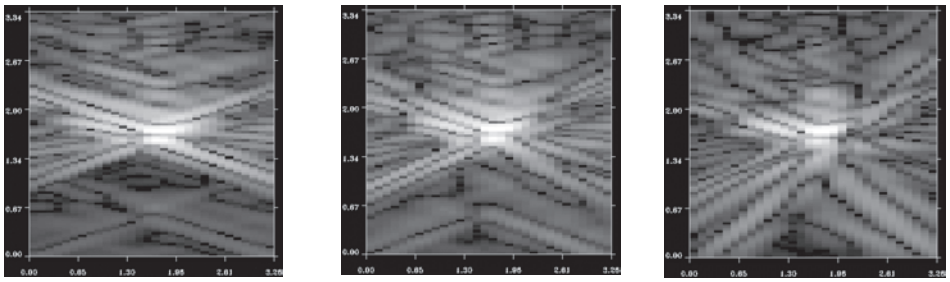


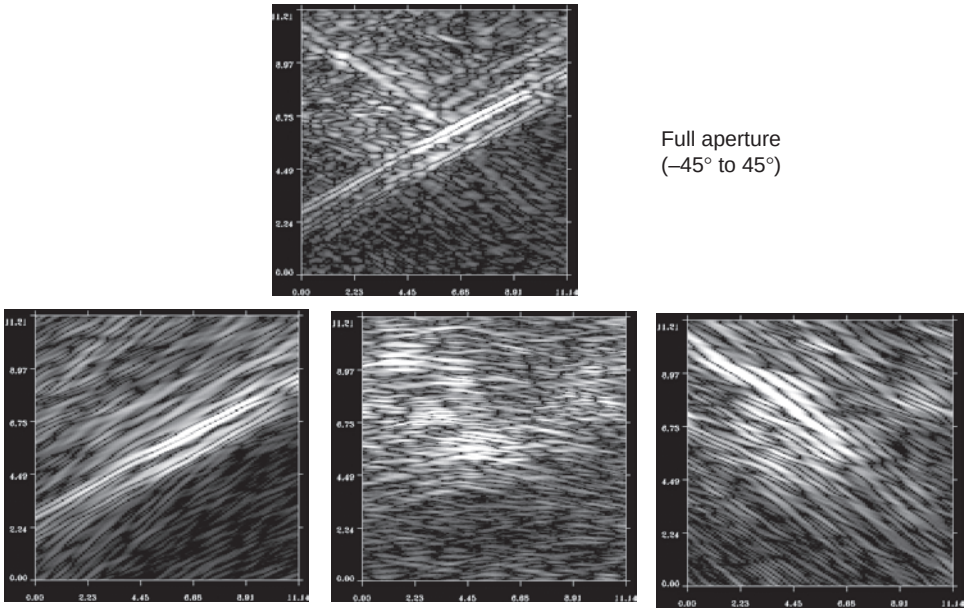


**Figure 25. Subaperture images of vehicle.**

For example, to produce the left-squinted image chip in figure 25, the left and right angles are set at 15° and 45°, respectively.

*Lever arm correction*.—The MOCOMP information provides the position of the antenna frame structure. ARL has used two transmit and two receive antennas to support a full polarization data set: VV, VH, HV, and HH. Since each antenna has a separate phase center, the MOCOMP information for each channel should be corrected according to the geometry of its transmit and receive antennas. The MOCOMP correction is required not only to produce a well focused image, but also to coregister image pixels from all different polarization channels. The user can select the Adjust

MOCOMP option and enter the $x$, $y$, and $z$ adjustments for lever arm correction. Note that the acquisition time $t$ is also needed to adjust the system delay timing in each channel.

*Aperture weighting*.—To reduce the sidelobe structure caused by the contribution from the two ends of the aperture, weighting is applied to the array of data to taper off the contribution. The radio selection box allows the user to select the aperture weighting type to form the image. There are three options available: rectangular, Hamming, and Hanning. Figure 26 shows the images of the same trihedral that are focused with and without aperture weighting.

Once the image is formed, it can be saved in either format—chip (CHP) format or bipolar image (BPL) format—by selecting the appropriate pushbuttons under the image area. The CHP format will be discussed in a later section. A number of data analysis functions are integrated in this software to support this data format.

### 2.1.2.8 *Pixel Tracking*

Pixel tracking is another data analysis and visualization technique that has been developed and integrated in the UWBView software package. This tool has played an important role and provided analysts with invaluable insights into UWB data analysis. Examples include understanding the effects of the motion compensation on SAR image quality, characterizing the antenna phase center, understanding the dispersion and diffraction effects associated with the UWB antenna pattern at different azimuth and depression angles, and developing the optimum integration angle for UWB SAR image formation. Given the coordinates of a pixel in the image area, the software goes back to the raw radar data domain and time shifts the return signals such that the centers of the data records are aligned with the pixel's phase center. The user can invoke this tool by selecting the SpotLight button from the PFDView menu (see fig. 27). The Pixel Tracking main window has the input parameter area and two plot windows. The input parameters are very similar to the parameters from the Image BackProjection menu. The first window displays the time-aligned raw data record corresponding to the pixel geometry profile. By the

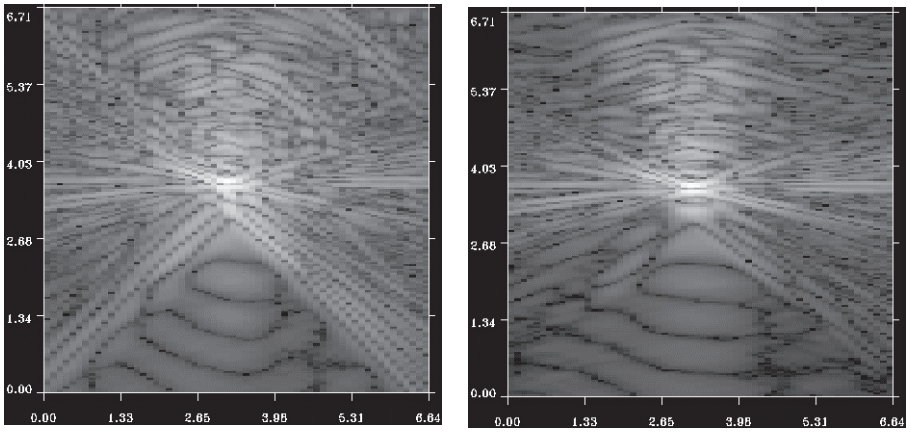


**Figure 26. 8-ft trihedral with rectangular and Hanning aperture weighting.**

notation given in the Image Formation section, each time-aligned data record in this view is $s_k(f(i, j, k) - R_G/2 : f(i, j, k) + R_G/2)$, where $R_G$ is the number of plotted range gates, $i$ and $j$ are the range and cross-range indices of the pixel to be tracked, $k$ is the aperture position index, and $f$ is calculated as in equation (4). These data records are displayed as a 2-D image, using color to encode the bipolar signals. (The encoding scheme was discussed in the Raw Image View section.) The second window contains two plots. The first plot shows the contribution to the image pixel at every aperture position. One can visualize this as the horizontal profile going through the center of the time-aligned 2-D image. The second plot shows the coherent integration of all the contribution along the aperture. The input parameters are described below.

*Pixel location*.—The $(x, y, z)$ coordinates for the pixel to be focused are required. This information can be entered if the user knows the exact location of the target. However, it is very difficult to know these coordinates, since a single target contains many pixels. In addition, we want to seamlessly visualize and relate information between the two domains—image and raw data. Thus, instead of entering the pixel location, the software offers a much more efficient approach: First, the user can invoke the Image BackProjection tool mentioned in previous section to form an image. Once the image is formed, the user can move the mouse pointer to navigate through the image. The textbox area below the image continuously displays the coordinates and value of the pixel indicated by the mouse pointer. By clicking the mouse button at any pixel, the user can export the $(x, y, z)$ coordinates of that pixel to the corresponding input controls of the Pixel Tracking menu. Then, when the Start button in the Pixel Tracking menu is pressed, the software will provide the corresponding data visualization in the raw data domain.

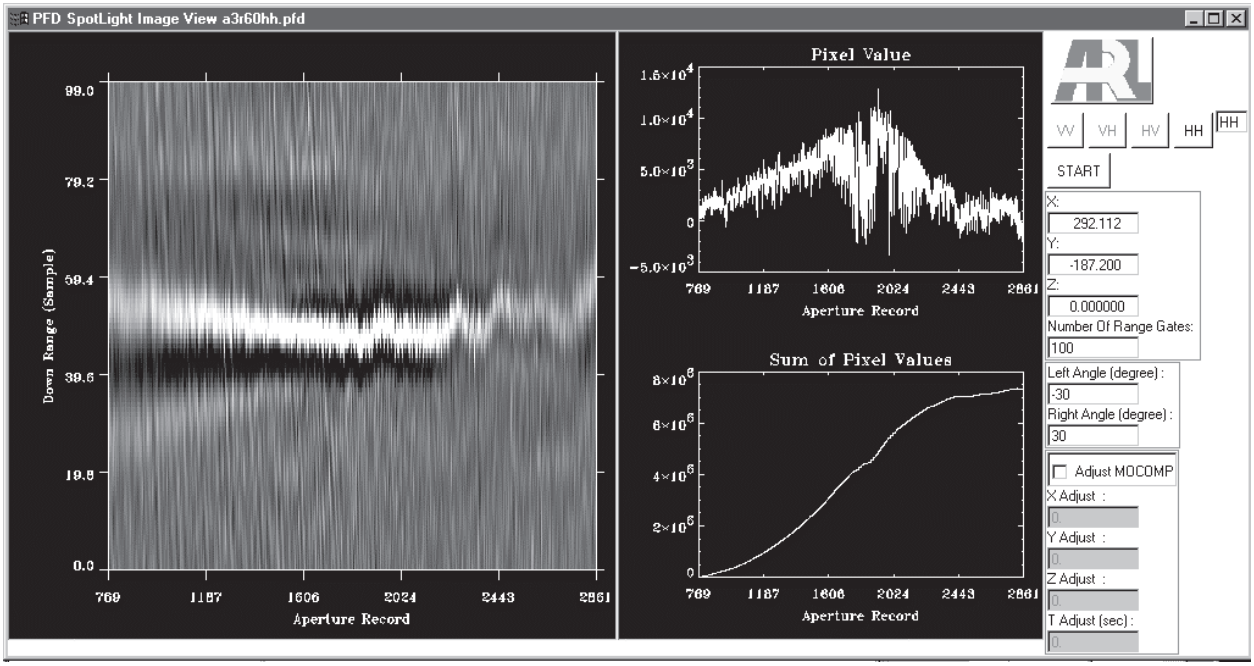


**Figure 27. Pixel tracking menu.**

*Number of range gates*.—This specifies the number of range gates included in the time-aligned 2-D image. Regardless of the number of range gates specified, the target response is always focused at the center of each range line record. The focus quality of the pixel only depends on the MOCOMP solution and the aperture.

*Aperture look angles*.—The left and right angle input parameters control the section of aperture that is used to focus the image pixel. This helps analysts to develop an understanding of the dispersion and diffraction effects associated with the UWB antenna pattern at different azimuth and depression angles, and to develop the optimum integration angle for UWB SAR image formation.

*Lever arm correction*.—This feature was previously discussed in the Image BackProjection section. However, it is used extensively in the Pixel Tracking menu as a primary tool to fine-tune the antenna phase center and system delay for each channel.

The MOCOMP information is used to perform the alignment. If the MOCOMP solution is not accurate (due to MOCOMP latency, inaccurate lever arm correction, or system delay, etc), the focus quality for the pixel will be degraded. This can be easily visualized using this analysis technique. In figure 28, the left image is an example of MOCOMP latency that has not been corrected. Note that the peaks of targets form a sine-wave-like path across the aperture due to the motion of the boomlift during travel. The right image of figure 28 shows exactly the same target response, but the MOCOMP latency has been corrected in this case.

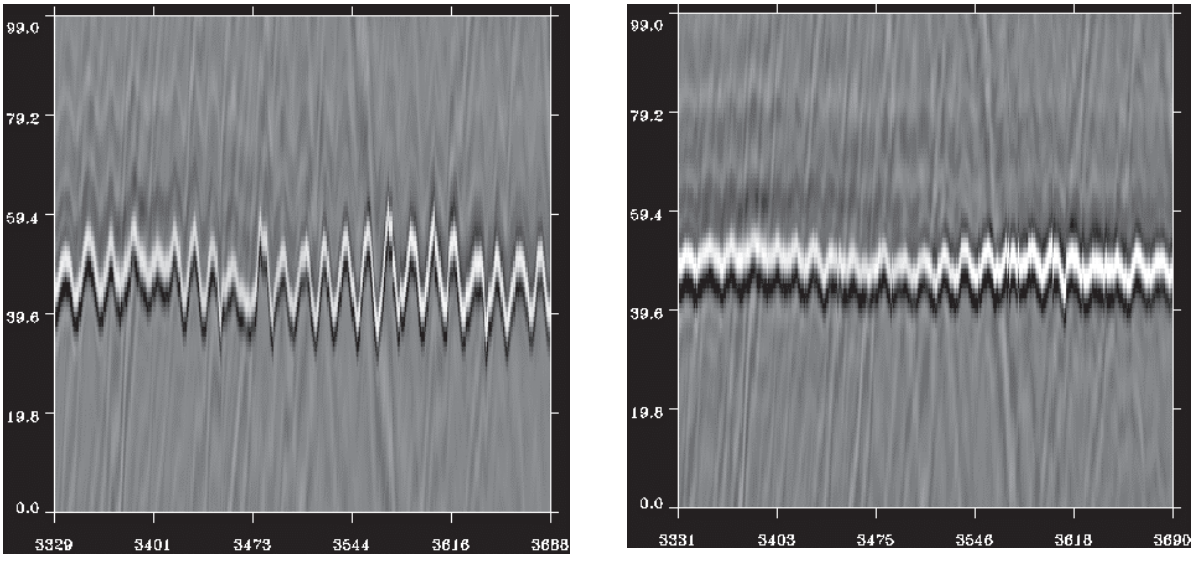


**Figure 28. Pixel tracking visualization of 8-ft trihedral before and after MOCOMP latency correction.**

## 2.2 Chip Data

### *2.2.1 Chip Data Description*

Detection and recognition techniques for UWB SAR radar are typically based on high signal-to-clutter ratio (SCR) and high SNR images. Figure 29 is a UWB SAR image from the Aberdeen Proving Ground data collection that shows many of the primary scattering mechanisms observed in low-frequency UWB data. The background is mainly tree clutter. Notice the spiky nature of forested clutter. There is a strong interaction between tree trunks and the ground, which forms a "dielectric" top-hat-type scatterer. This leads to tightly focused, bright returns in the image. Those on the lower right-hand corner of figure 29 are some of the tactical targets.

There is an interaction between vehicle sidewalls and the ground, which forms dihedral-like scatterers. Vehicles have long linear elements and distributed responses due to their complex physical outlines. Open areas primarily absorb or forward-scatter incident radiation, leading to very low levels of backscatter. To support the phenomenological study and development of target/clutter discrimination features, we extract images from the areas of interest and construct image chip databases. The chips are segregated into target versus confuser categories. One can select areas of interest, either manually or with the help of a prescreener that canvasses through a large image area and generates coordinates of targets and difficult clutter. With the chip creation tool, image chips that correspond to points of interest are extracted from large images and packaged into a chip file. Currently, this chip creation tool is a stand-alone application; it should be integrated into UWBView in the future. Once the chip file is constructed, it can serve in two different areas of study: the phenomenological study of target/clutter discrimination features, and the implementation and detection of algorithms.

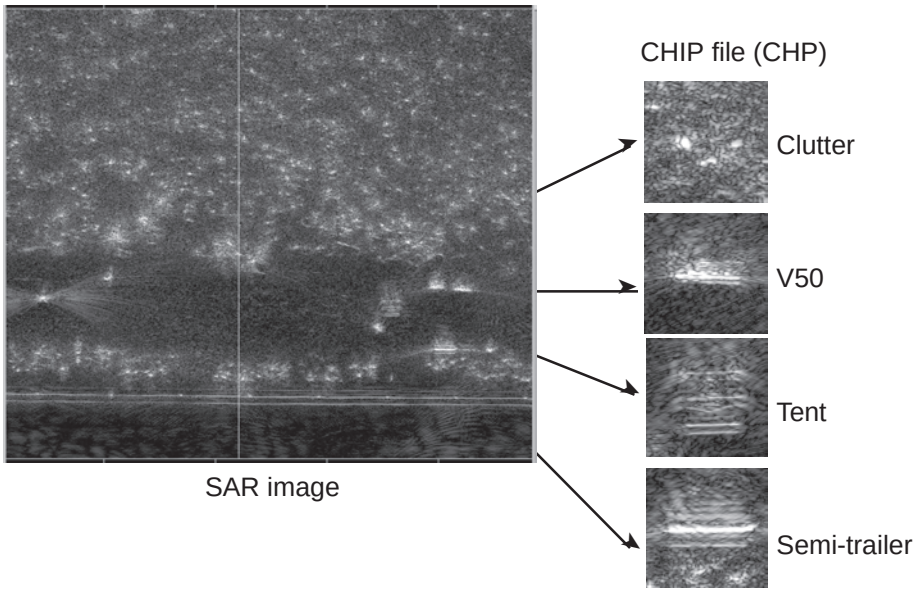


**Figure 29. Sample image from APG III data collection. Image chips are extracted and saved into CHIP file for analysis.**

The UWBView software is used primarily to investigate potential target/clutter discrimination features. It allows the user to randomly access any chip from a CHP file, visualize it, and use a number of built-in analysis functions to study its properties. The chip database is also employed during the implementation phase of discrimination feature. An application programming interface (API) has been developed that allows algorithms to access images from chip database to evaluate their discrimination features. This API supports both UNIX and Windows NT operating systems. Any differences in CPU data representation is handled by the API library and transparent to the programmer.

Table 2 lists the contents of a CHP file. The file contains a volume header, followed by the image chips. The first word of the volume header is a "magic number," used to indicate that this is a CHP file. This magic number is also useful to determine whether the CPU data format (little-endian or big-endian) matches the file data format. At run time, the program reads in the first four bytes from the file and compares them with the known magic number. If the input bytes have to be swapped to match the magic number, then any subsequent reading from the file also requires swapping accordingly. The second word of the file is the volume

**Table 2. CHP file format.**

| Name | Description | Data type | Number of elements |
|---|---|---|---|
| MAGIC | Magic number to identify as a CHP file | 32-bit long integer | 1 |
| SIZE_VOLHDR | Size of volume header (in bytes) | 1 | 1 |
| BASE | Run identification | ASCII | 80 |
| N_CHIP | Number of chips in file | 32-bit long integer | 1 |
| R_INCREMENT | Pixel spacing (in meters) in range direction | Float | 1 |
| XR_INCREMENT | Pixel spacing (in meters) in cross-range direction | Float | 1 |
| N_R | Number of pixels in range direction | 32-bit long integer | 1 |
| N_XR | Number of pixels in cross-range direction | 32-bit long integer | 1 |
| SIZE_CHIPHDR | Size of chip header | | |
| GT_CODE1 | Ground truth Code level 1 | ASCII | 80 |
| GT_CODE2 | Ground truth Code level 2 | ASCII | 80 |
| POI_CENTER_X | Chip center $x$ | Float | 1 |
| POI_CENTER_Y | Chip center $y$ | Float | 1 |
| POI_CENTER_Z | Chip center $z$ | Float | 1 |
| CHIP_DATA | 2-D chip image | Float | N_R*N_XR |

header size. This word contains the pointer to the first image chip. If the volume header of CHP file has to be extended in subsequent software revision, the old software still works with new data file with the volume header size information. Other information in the volume header is described in table 2.

Following the volume header is the first image chip. Each chip contains a header describing the object in the image. Similar to the volume header, the chip header also includes the image's size, to allow for a software upgrade. The location ($x$, $y$, $z$) of the chip center is also included in the chip header. The ground truth information associated with the image chip is included and has two parts: level 1, which classifies the object (vehicle, mine, man-made object, canonical scatterer, or clutter), and level 2, which describes the object in more detail.

### 2.2.2 *CHP Data Analysis*

To access a CHP file, select the Open CHP File menu item. The file selection window lets the user either enter the filename or browse through the file system and select the CHP file. Since the UWBView software supports data sets with four polarization channels, a file name convention is needed. Each CHP file name must include at least two special characters—*vv*, *vh*, *hv*, or *hh*—that label the corresponding polarization channel. The position of this polarization label in the filename is not important. However, the four CHP files of the same data set must have the same filename, except for the polarization label. For example, the four filenames for a data set might be A4R109m1vv.chp, A4R109m1vh.chp, A4R109m1hv.chp, and A4R109m1hh.chp. This is the filename convention for real images (ARL's UWB data). In addition, the software also supports complex images (RASTR and P3 data). In this case, the polarization label is appended with either *i* for in-phase or *q* for quadrature. Thus, the required label set will include *vvi*, *vvq*, *vhi*, *vhq*, *hvi*, *hvq*, *hhi*, and *hhq*.

Although there are several CHP files that compose a single data set, the user only needs to select any one file in the data set. The software will examine the directory for available polarization channels to determine whether this data set contains real or complex images and to access the files properly.

Once the CHP file is opened, the file information can be viewed by selecting CHIP File Information from the CHIPView menu (see fig. 30). The user can also view the file contents by selecting CHIP Listing from the CHIPView menu. Figure 31 shows the CHIP Listing window. Each chip has an index, its groundtruth labels, and its location. The chip index is used to randomly access any chip in the file and display its image. This feature will be discussed shortly.

Figure 32 shows the Chip Image View main window. To invoke this window, select Chip Image from the CHIPView menu. The Chip Image View window has a graphic area to display the chip image, and other controls to obtain input from the user and display chip-related

**Figure 30. Chip file information.**

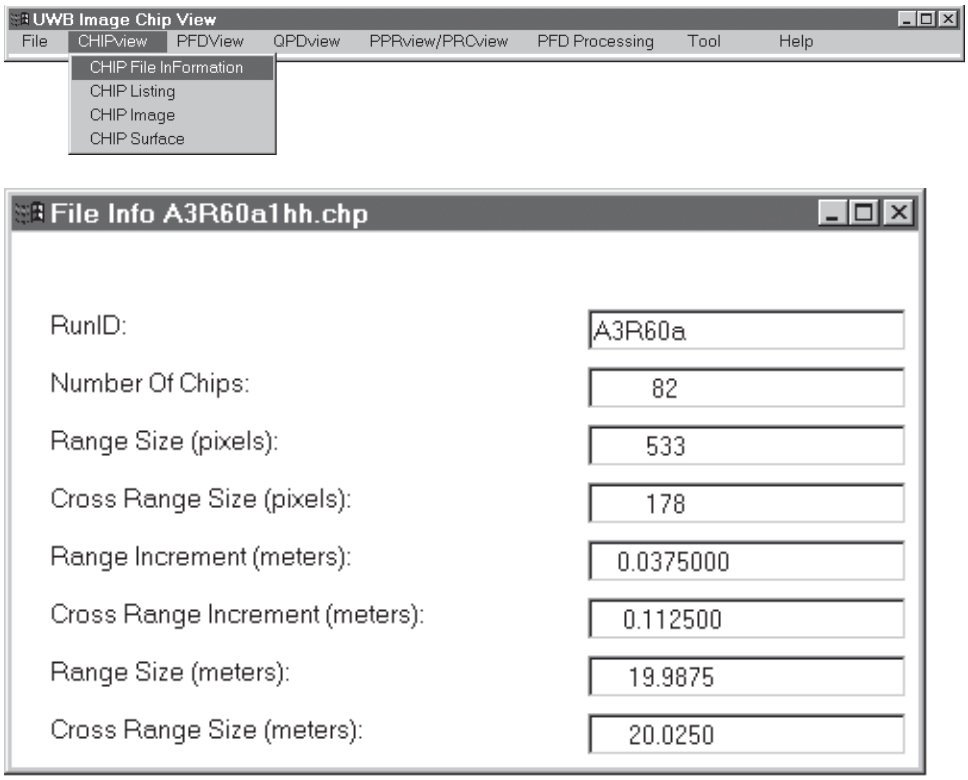


**Figure 31. Chip listing.**

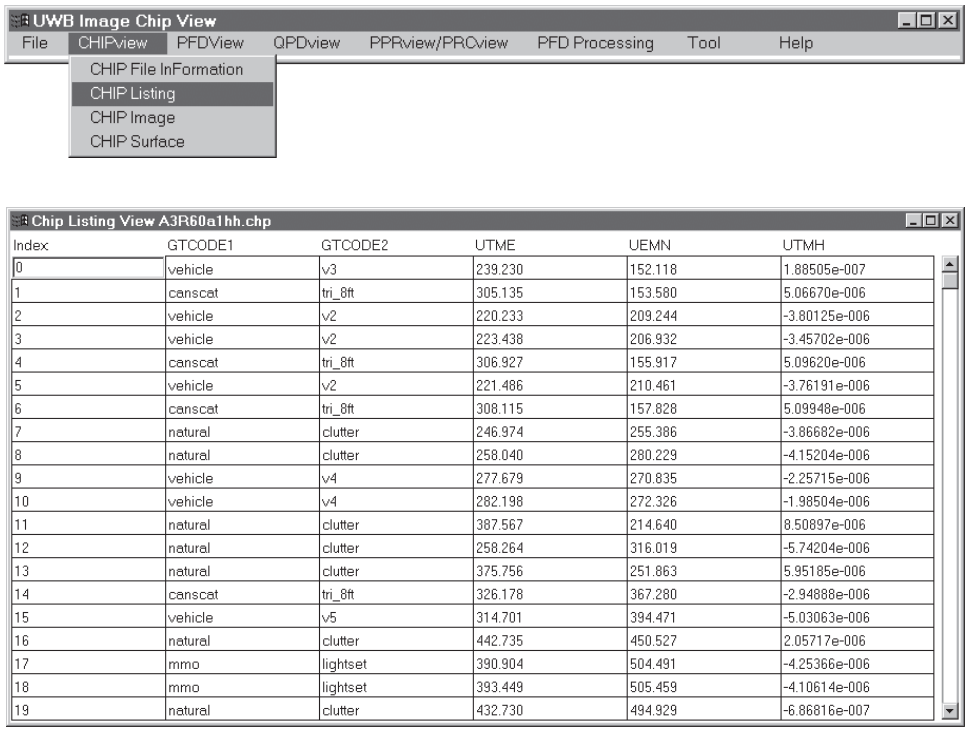


| Index | GTCODE1 | GTCODE2 | UTME | UEMN | UTMH |
|---|---|---|---|---|---|
| 0 | vehicle | v3 | 239.230 | 152.118 | 1.88505e-007 |
| 1 | canscat | tri_8ft | 305.135 | 153.580 | 5.06670e-006 |
| 2 | vehicle | v2 | 220.233 | 209.244 | -3.80125e-006 |
| 3 | vehicle | v2 | 223.438 | 206.932 | -3.45702e-006 |
| 4 | canscat | tri_8ft | 306.927 | 155.917 | 5.09620e-006 |
| 5 | vehicle | v2 | 221.486 | 210.461 | -3.76191e-006 |
| 6 | canscat | tri_8ft | 308.115 | 157.828 | 5.09948e-006 |
| 7 | natural | clutter | 246.974 | 255.386 | -3.86682e-006 |
| 8 | natural | clutter | 258.040 | 280.229 | -4.15204e-006 |
| 9 | vehicle | v4 | 277.679 | 270.835 | -2.25715e-006 |
| 10 | vehicle | v4 | 282.198 | 272.326 | -1.98504e-006 |
| 11 | natural | clutter | 387.567 | 214.640 | 8.50897e-006 |
| 12 | natural | clutter | 258.264 | 316.019 | -5.74204e-006 |
| 13 | natural | clutter | 375.756 | 251.863 | 5.95185e-006 |
| 14 | canscat | tri_8ft | 326.178 | 367.280 | -2.94888e-006 |
| 15 | vehicle | v5 | 314.701 | 394.471 | -5.03063e-006 |
| 16 | natural | clutter | 442.735 | 450.527 | 2.05717e-006 |
| 17 | mmo | lightset | 390.904 | 504.491 | -4.25366e-006 |
| 18 | mmo | lightset | 393.449 | 505.459 | -4.10614e-006 |
| 19 | natural | clutter | 432.730 | 494.929 | -6.86816e-007 |

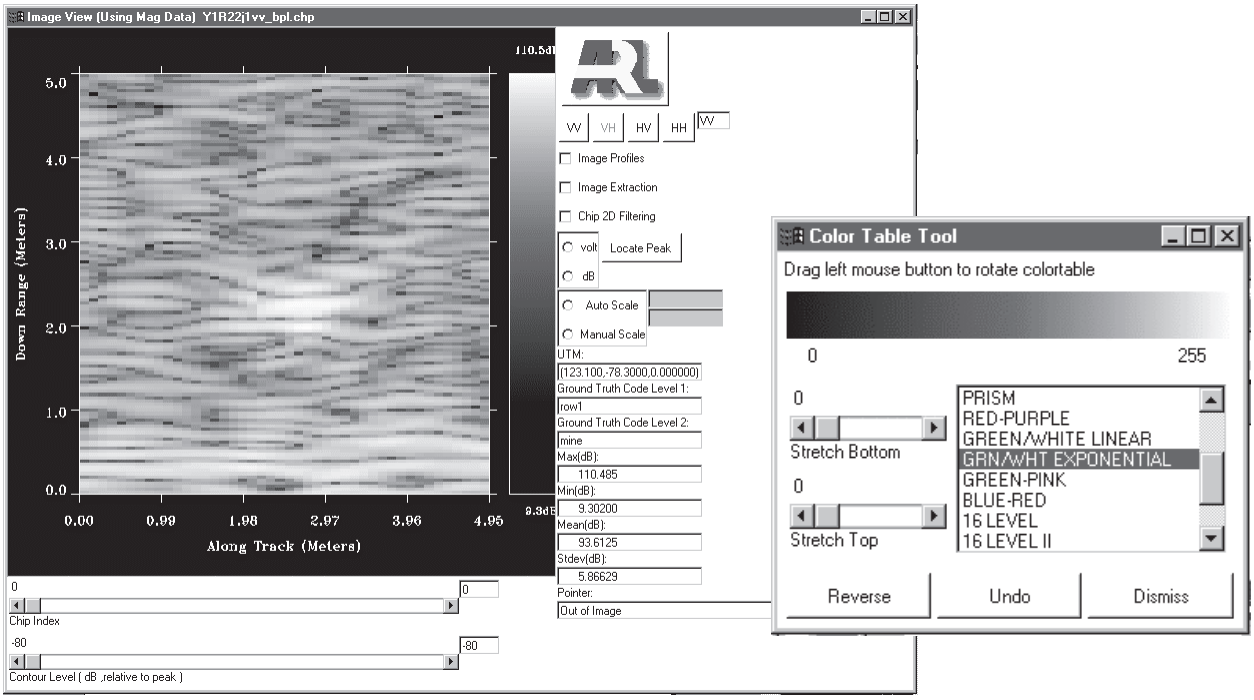


**Figure 32. Chip image view.**

information. The image is color encoded using the image amplitude in decibels. For a real image (e.g., ARL's UWB data), the magnitude is computed as

$$\mathrm{mag}_i = 20\log_{10}(|I_i|),$$

where $I_i$ is the bipolar value of the $i$th pixel.

For a complex image (e.g., RASTR and P-3 data), the magnitude is computed as

$$\mathrm{mag}_i = 20\log_{10}\left(\sqrt{I_i^2 + Q_i^2}\right),$$

where $I_i$ and $Q_i$ are the in-phase and quadrature components of the $i$th pixel, respectively.

Since we are using 8-bit color to encode the image amplitude, the color index of $i$th pixel is

$$P_i = 255\frac{\mathrm{mag}_i - \min}{\max - \min},$$

where max and min (in dB scale) determine the dynamic range for viewing the image. The UWBView software provides two options. When the user selects the Auto Scale option, min and max are the actual minimum and maximum values of the image chip. This option is used most often to view images, since the entire image's dynamic range is mapped into the available color space. The user can also select the Manual Scale option. In this mode, the user supplies the minimum and maximum values. This option is used to keep the dynamic range of the displayed image constant and is desirable in case multiple image chips are to be evaluated and compared. In any case, the effective dynamic range of the displayed

image can be quickly changed using the Color Table Tool, which can be invoked by selecting the Color Tool button from Tool menu. The Color Table Tool window has 17 built-in color maps and allows the user to interactively modify a color map. The Stretch Bottom and Stretch Top slider controls are used to linearly expand the range of color table indices, thus effectively changing the viewable dynamic range of the image.

The text controls on the right of the image area are used to list the information associated with the displayed chip: coordinates of chip center, ground truth labels, and standard image statistics (minimum, maximum, mean, and standard deviation).

The user can navigate through the image using the mouse pointer. The coordinates and value of the pixel indicated by the mouse pointer are continuously updated. This is a very useful feature, where the user can measure the amplitudes of various scatterer components of an object. The Locate Peak button is used to identify the brightest pixel in the image. The intersection of the vertical and horizontal lines is the location of the peak pixel.

There are two slider controls located below the image area. The bottom slider (see fig. 32) is used to display the contour on top of the image. The user must specify the contour level in decibels with respect to the peak of the image (0 dB). The range and cross-range resolutions of the radar can be measured using this feature. Figure 33 shows an example where two contours (3 and 6 dB) are overlaid on top of the chip image of a trihedral. The top slider is used to randomly access any image chip. The Chip Listing (see fig. 31) is needed to preview the contents of the file and look up the desired chip index.

The four buttons—VV, VH, HV, and HH—provide seamless switching between the polarization channels. This feature provides a very useful tool in the development of polarization features for target/clutter discrimination. When the user selects a chip file for analysis, the software examines the directory for all available polarization channels. Each polarization selection button is enabled only if the underlying data for that particular channel are available.

The Image Extraction main window (see fig. 34) provides further image analysis functions. This window is created when the Image Extraction input box from the Chip Image window is selected. The window is provided for two main reasons: to extract a small area from the image chip and analyze this subimage. An image chip might contain scattering components from the object, resonance behind the object, and surrounding clutter. Thus, the extraction is needed so that the analysis functions can be performed on the desired image area. When the Image Extraction main window is created, the user can use the mouse to drag a rectangular region in the Chip Image display window. The selected image area will be displayed in the Image Extraction graphic window. The standard statistics (minimum, maximum, mean, and standard deviation) for the extracted image are updated when a new area is selected. As the mouse pointer moves across the extracted image, the coordinates and value of

**Figure 33. 3- and 6-dB contours overlaid on 8-ft trihedral image.**

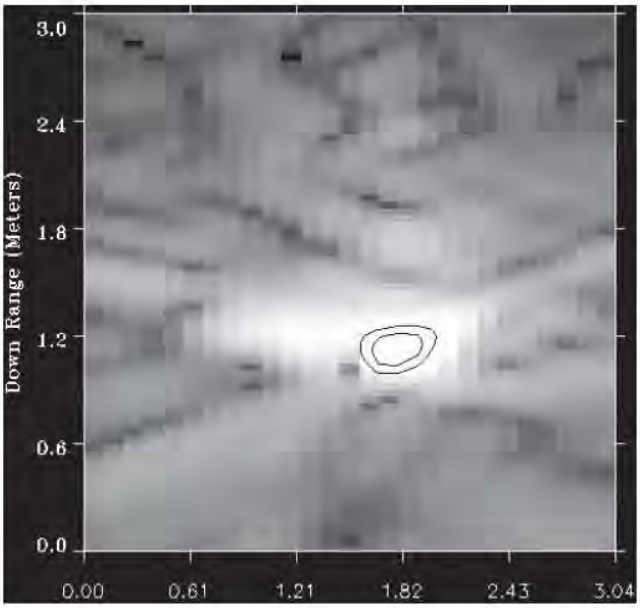


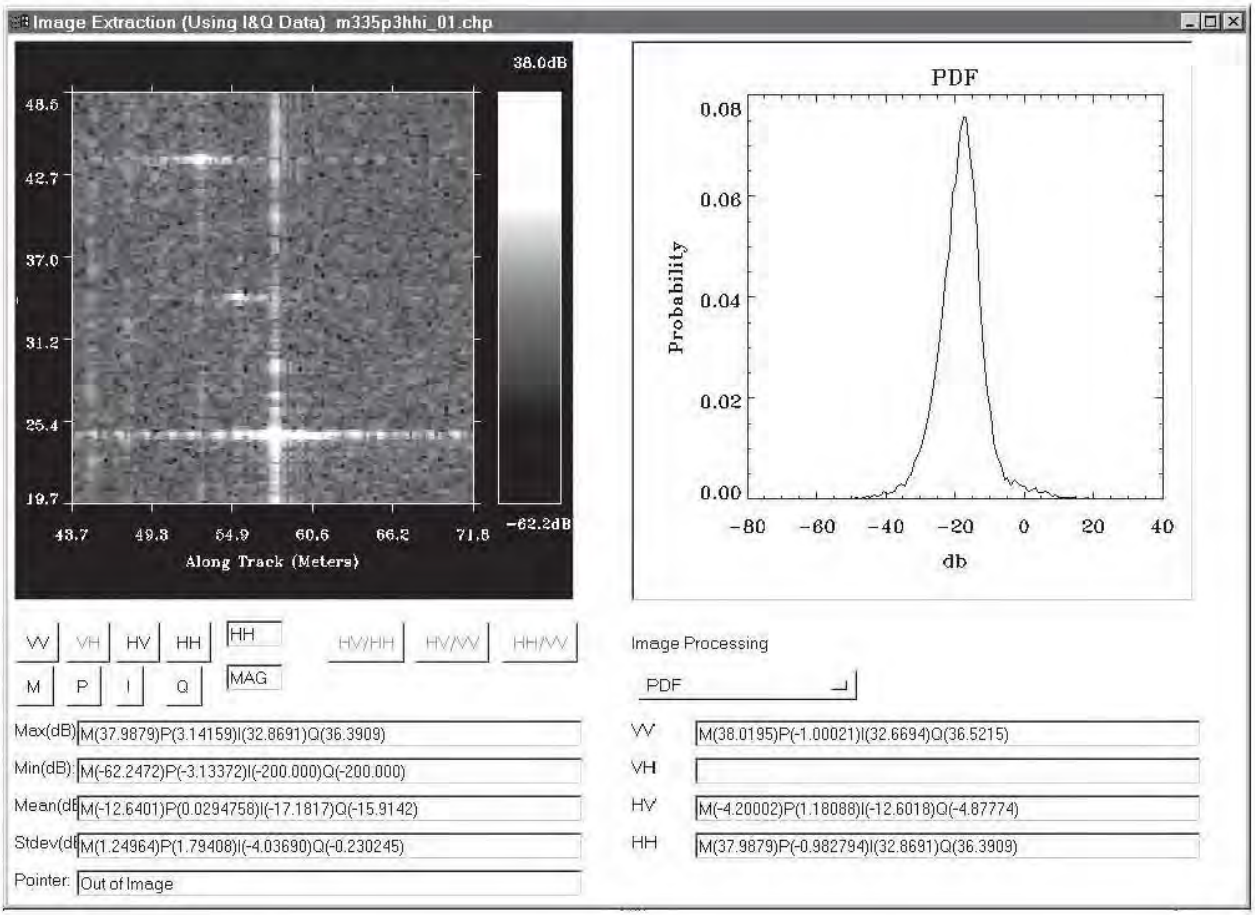


**Figure 34. Image extraction window.**

the pixel are continuously updated and displayed in the Pointer output textbox. Similar to the Chip Image window, the Image Extraction window also provides access to all available polarization channels. The polarization selection buttons are independent from the ones in the Chip Image window. That means the polarization of the extracted image depends on the current selection in the Image Extraction window, not the Chip Image window. Using this feature, one can easily evaluate the polarization channel alignment, which is the requirement for polarization processing algorithms. This also helps in the analysis and development of polarization-based discrimination features.

While the Chip Image window can only display the magnitude image, the Image Extraction window can display the image using any of the following data representations: M (magnitude), P (phase), I (in-phase), or Q (quadrature). Note that the statistics output textboxes are always updated corresponding to the data type being viewed. The data type selection buttons (M, P, I, or Q) are only enabled if the underlying data are complex.

There are several processing functions that operate on the extracted image. They can be accessed using the Image Processing pull-down menu. Most analysis functions output results to the second graphic window in the Image Extraction main window. This image processing list will be extended to support other processing requirements. Following are the processing functions that are currently implemented.

#### 2.2.2.1 *Probability Density Function (PDF), Cumulative Distribution Function (CDF), and Exceedance Function (EXDF)*

Select the PDF button from Image Processing pull-down menu to generate the PDF of all pixels from the extracted image (see fig. 34). The image amplitude is converted to log magnitude, and its histogram is computed to generate the PDF curve. This allows studies of distribution functions for various types of objects (forest area, open field area, vehicles, etc). This knowledge is important in the development of target/clutter discrimination algorithms. Figure 35 shows the PDF, CDF, and EXDF functions of the extracted image in figure 34.

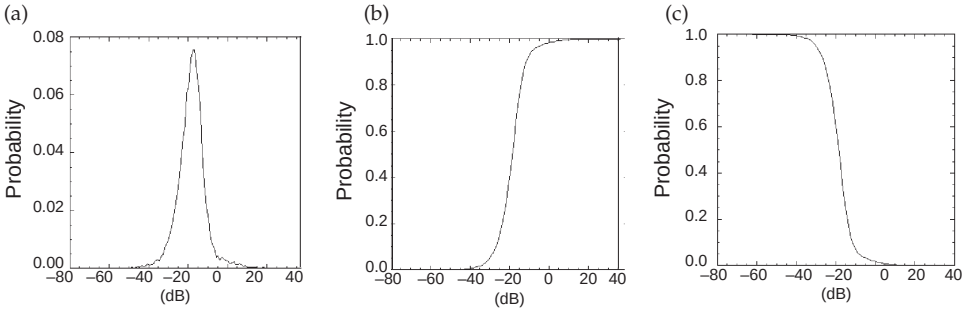


**Figure 35. (a) PDF, (b) CDF, and (c) EXDF of extracted image in figure 33.**

### 2.2.2.2 *Down-Range Profile and Spectrum*

This feature allows us to extract a down-range line from the image and examine its spectral content. When this option is selected, every time a mouse pointer is clicked at the extracted image, the corresponding down-range profile from the image and its spectral content are plotted in the output window (see fig. 36). The spectral property plays an important role in detection and recognition of targets in UWB radar. Figure 37 shows an example where the spectral content is the key feature for discriminating a mine from a confuser. In the image domain, a mine has a very similar shape and amplitude when compared to other objects in the clutter area. However, in the frequency domain, a mine has a unique spectral content that allows us to differentiate it from other objects. ARL has been employing this to implement the mine-detection algorithm for UWB radar [8].

**Figure 36. Down-range profile and spectrum.**

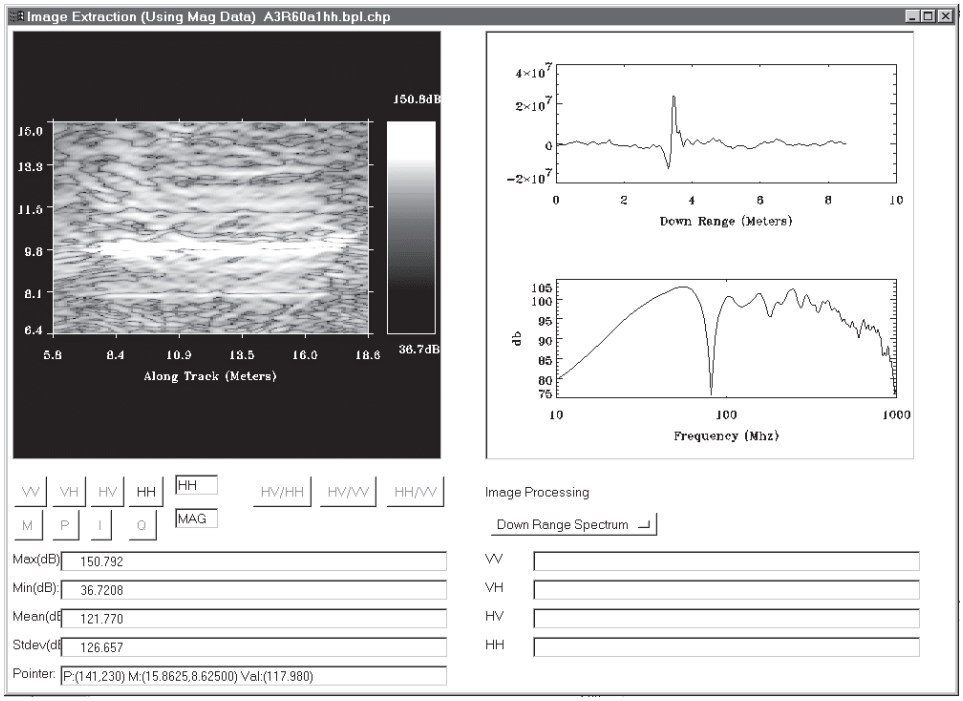

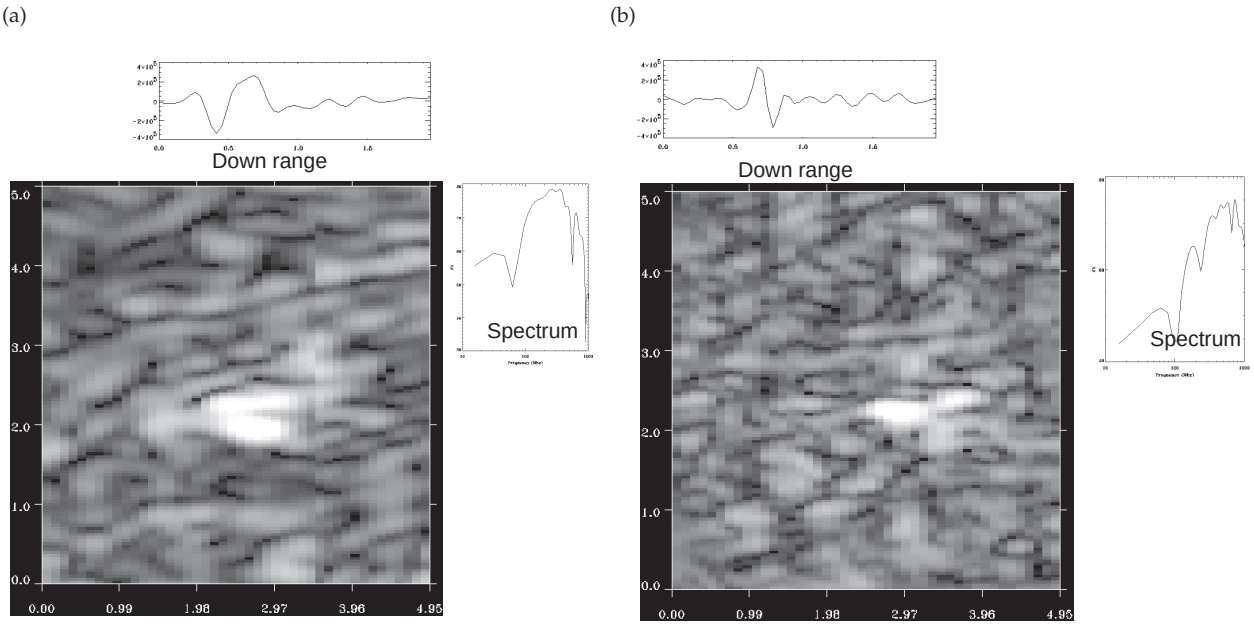


**Figure 37. Down-range profile and spectrum of (a) mine and (b) clutter.**

#### *2.2.2.3 1-D Spectral Content of Image*

In the visualization of figure 38a (see p. 32), the spectral content of every down-range profile of the extracted image is computed and displayed using a false color plot. Figure 38b illustrates the procedure, in which each down-range profile from the bipolar image is extracted and its corresponding spectral content is computed using a fast Fourier transform (FFT). All the spectral lines form an ensemble image, using color to encode the amplitude. This allows the user to visualize the variance of the object's spectral content with different cuts through its image.

#### *2.2.2.4 2-D Spectral Content of Image*

This option transforms the extracted image into its frequency-space domain (see fig. 39 on p. 32). This representation allows us to isolate and visualize the angle- and frequency-dependent scattering phenomenon of targets. Figure 40 (on p. 33) shows the image of a trihedral and its 2-D spectral content. Since the trihedral is an isotropic target, its spectral has nearly uniform distribution with respect to aspect angle. Figure 41 (also on p 30) shows the image of a vehicle and its 2-D spectral content. The frequency-space domain shows that the target has a strong response at a preferred aspect angle. Since the angle- and frequency-dependent scattering phenomenon of targets can be discovered in this domain, ARL has started investigating the formulation of some decision statistics deriving from this domain that could provide potential target/clutter discrimination.

**Figure 38. 1-D spectral content of image: (a) image of vehicle and its 1-D FFT visualization and (b) procedure for visualizing 1-D FFT from image chip.**

(a)

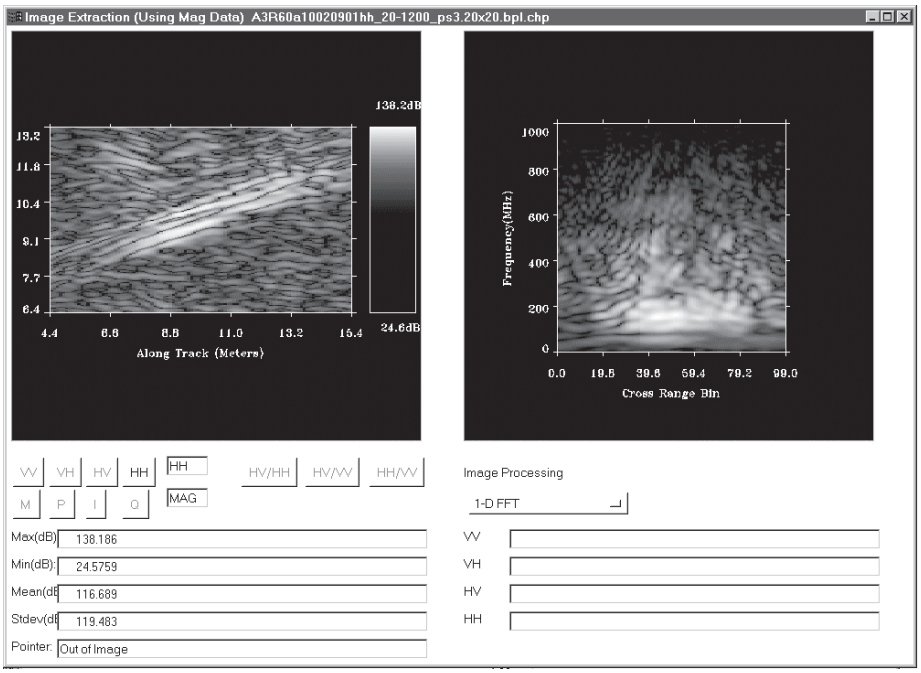


(b)

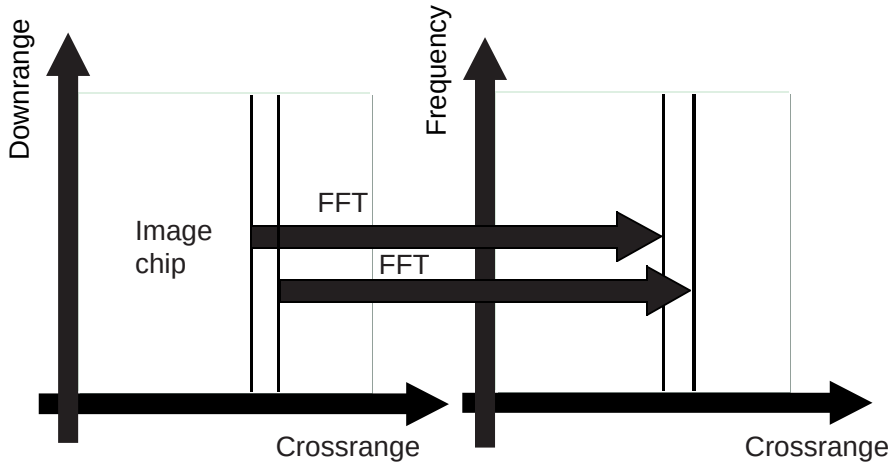

**Figure 39. Image of vehicle and its 2-D FFT visualization.**

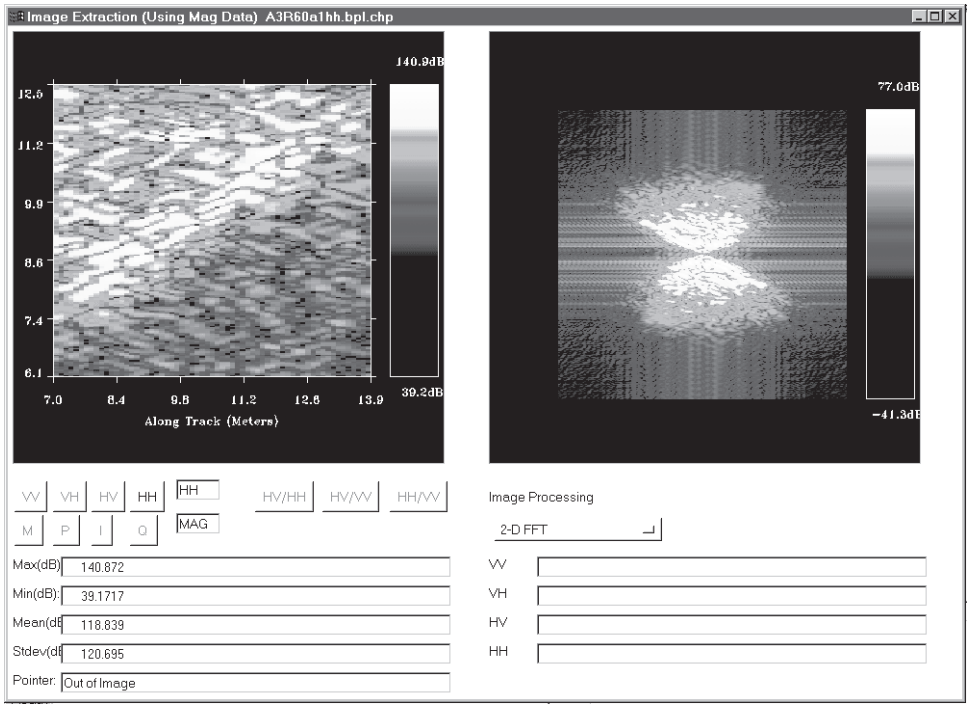


**Figure 40. Image of 8-ft trihedral and its frequency-space domain representation that shows its response is nearly uniform with respect to aspect angle.**

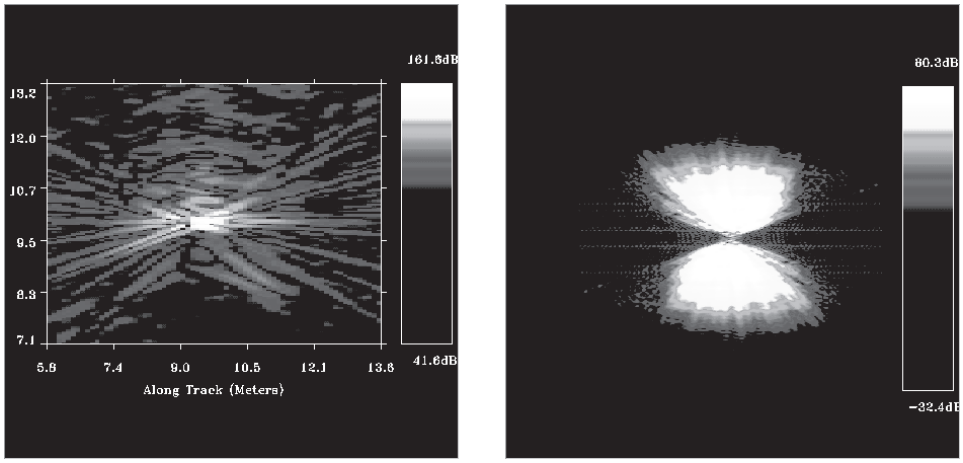


**Figure 41. Vehicle and its frequency-space domain representation. Note that vehicle "flashes" at broadside.**

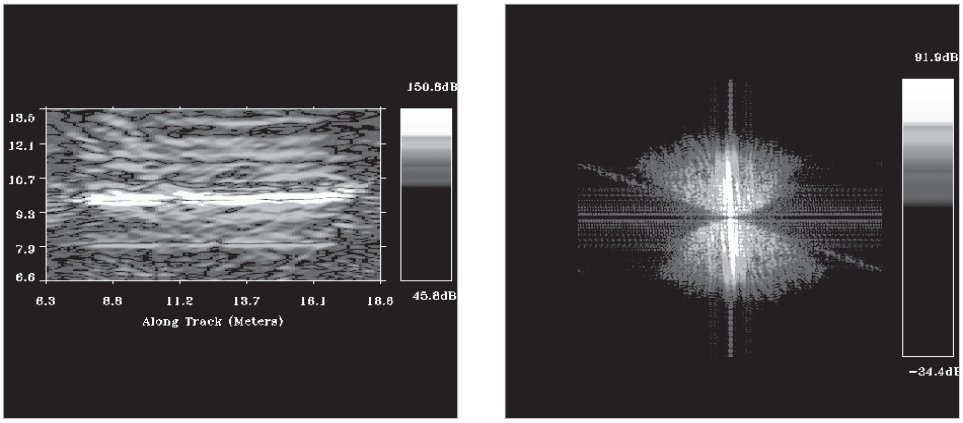

### 2.2.2.5 *Image Post-Processing*

Traditionally, radar data have been processed in the raw domain before the image is formed. For example, we have incorporated the frequency- and angle-dependent features into our detection algorithm to detect vehicles from clutter [7]. In order to extract frequency- and aspect-dependent features, raw data must be reprocessed for the required frequency subbands, and images must be refocused to produce the required subbanded and subaperture images. This approach has severe disadvantages in the computational requirement. Georgia Tech has shown that many important preprocessing techniques can be implemented as equivalent linear shift-invariant post-filtering in the image domain [9]. This leads to a significant savings in computational requirements. Using the Georgia Tech filter design software [10], one can design a 2-D subband, subaperture, or combination of subband and subaperture filter. Future work will include the post-filter for focusing the resonance signature, as well [11]. Once the 2-D filter coefficients are generated (using the Georgia Tech filter design software), the UWBView software performs the application of the filter on the image chips. By selecting the radio button in the chip display window (see fig. 32), the Chip 2-D Filter window will pop up (see fig. 42). After the Load Filter pushbutton is invoked, the user can select the 2-D filter file. Since the filtering process is implemented in the frequency domain, the software reads in the 2-D filter coefficients and performs a 2-D FFT operation. This computation is performed once and the 2-D FFT of the coefficients is used to apply to any selected image chip until another filter is loaded. After the filter file is selected, the two plots in the left column of the Chip 2-D Filter window will show the impulse

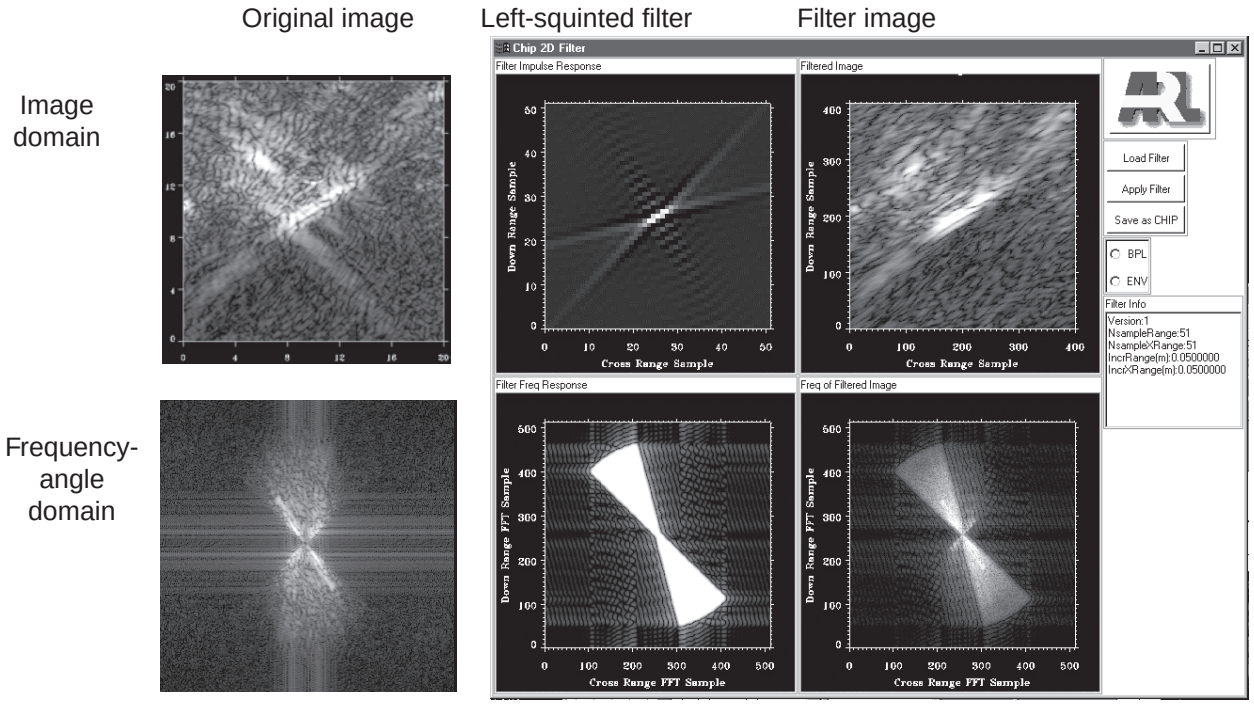


**Figure 42. Chip 2-D filter menu.**

response and the frequency response of the 2-D filter, respectively. The Filter Info textbox also shows more information about the filter, such as the number of pixels and the spacing in range and cross-range dimensions. As described in the previous section, the user can randomly access any chip in the CHP file using the Chip Index slider control in the Chip Image View window. Once the filter is loaded and a chip is selected, the Apply Filter pushbutton in the Chip 2-D Filter window can be invoked to filter the current chip. The two plots in the right column of the Chip 2-D Filter window will show the resulting image chip and its 2-D frequency content. The filtered image can be saved into a CHP file by invoking the Save as Chip button.

To demonstrate that the post-filtering technique is equivalent to the preprocessing scheme, we selected a small area from APG III data collection and performed subband and subaperture processing using both techniques. This area includes a vehicle with noncardinal orientation and tree clutter. This configuration is appropriate for demonstrating both frequency- and aspect-angle dependency features. The original image chip is focused using the backprojection tool described in the previous section. Figure 43 shows the image chip focused using this tool. The

**Figure 43. Using backprojection tool to form original image.**

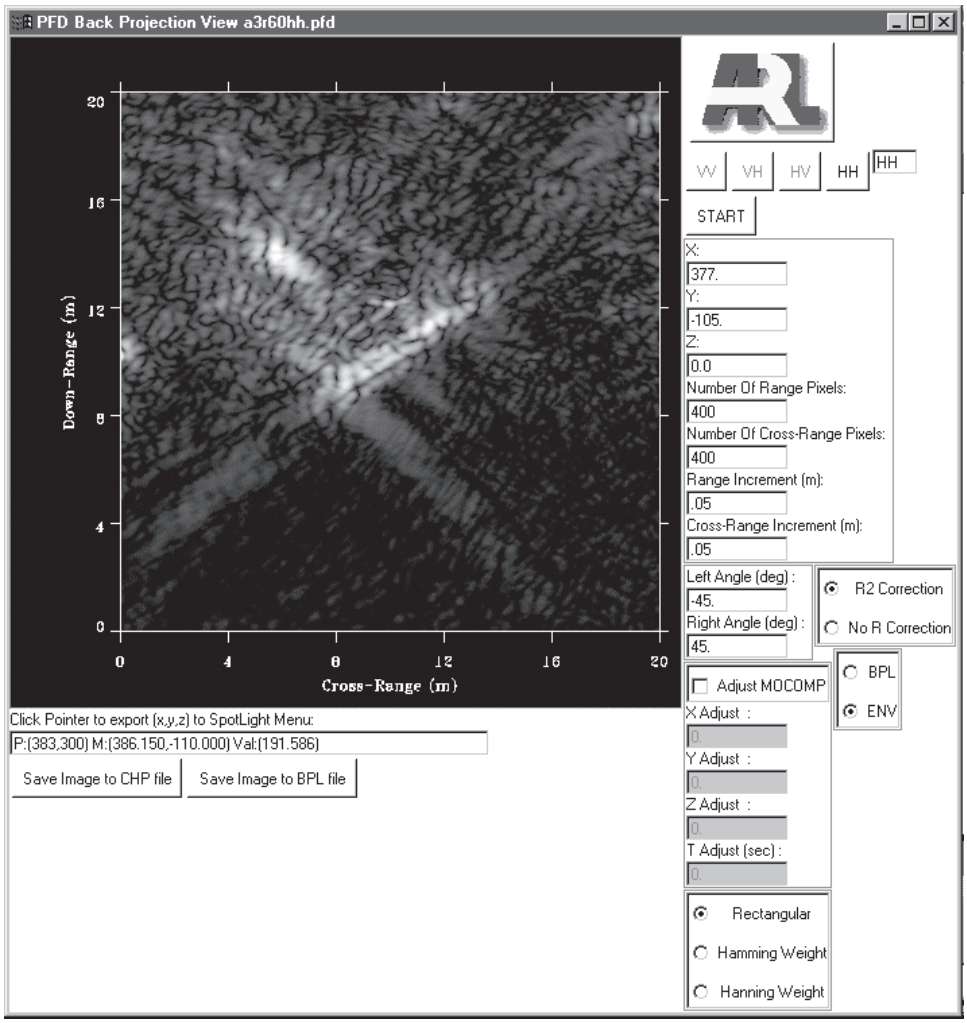

image is focused using a 90° integration angle with rectangular aperture weighting. The spacing is set at 5 cm for both the down-range and cross-range directions. This is equivalent to a sampling rate of 3 GHz, which is adequate for the signal bandwidth of 1.2 GHz. For subband preprocessing, we designed three bandpass filters (100–200 MHz, 200–500 MHz, and 700–1000 MHz), used the filtering tool (see fig. 21) to filter down-range data, and used the backprojection tool to generate subband images. For subaperture preprocessing, we used the backprojection tool to generate three subaperture images. The left angle and right angle parameters in the backprojection tool allow appropriate subaperture focusing. The parameters for the three subapertures are –45° to –15°, –15° to 15°, and 15° to 45°. For post-processing, we designed six 2-D postfilters, three for frequency subbanding and three for subaperture processing. The postfilters are all 51 × 51 in size. These postfilters are then applied to the original image to produce the corresponding subband and subaperture images. Figures 44 and 45 show the subband and subaperture images using both techniques. The figures show very good agreement between the two techniques.

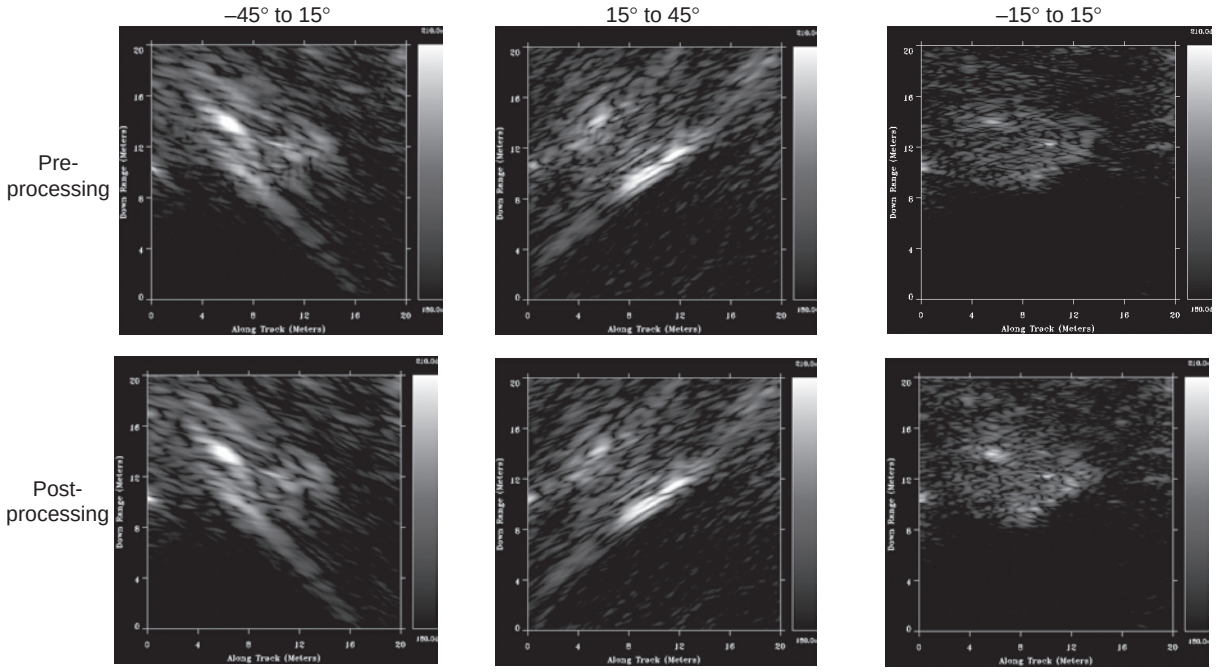


**Figure 45. Subaperture images using both pre-processing and post-processing techniques.**

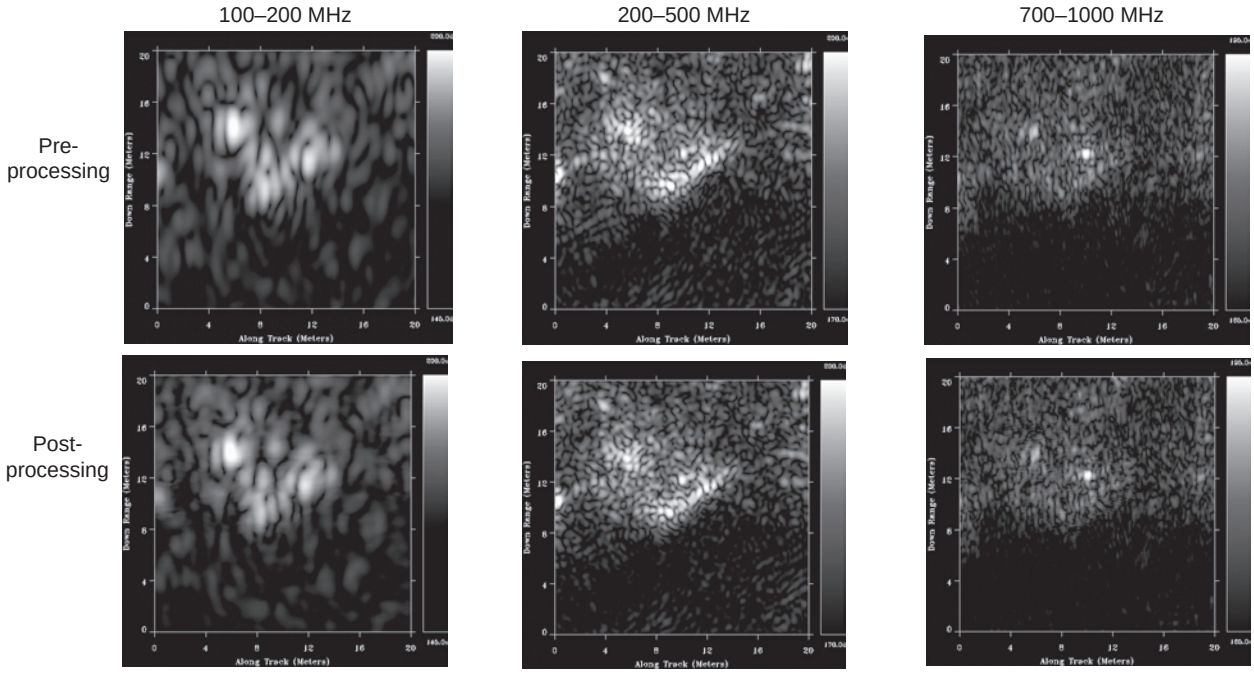


**Figure 44. Frequency subbanding images using both pre-processing and post-processing techniques.**

#### *2.2.2.6 Pixel Values from All Polarization Channels*

The investigation of the polarization isolation requires the comparison of image pixel value across all channels. This option displays the values of the same image pixel from all available polarization channels. Clicking the mouse at any pixel in the extracted image updates the pixel values in the textboxes labeled VV, VH, HV, and HH, below the graphic output window (see fig. 34 on p. 29).

# 3. Summary

The software package UWBView provides a critical toolkit for phenomenological studies of UWB SAR data and imagery. It has been employed extensively for data analysis and processing, especially in the developments of target/clutter discrimination features. Although the software was developed to support the ARL UWB program, its application has been extended to other data as well, such as P-3, CARABAS, and RASTR data. However, there is much work to be done to improve its usefulness and to satisfy the new ideas and requirements of a research environment. The processing modules in figure 1 should be ported and integrated into UWBView to provide a seamless data production environment. Following are some features that should be available in the future.

*Radio frequency interference removal.*—There are two RFI algorithms that are currently available as stand-alone applications. The first one is the Chirp-Z Least-Squares with Target Excision (CLSX) algorithm (developed by ARL and Ohio State University), which has been used to produce ARL imagery. The second algorithm (developed by ARL and GORCA, Inc.) generates adaptive finite impulse response (FIR) filters to whiten the interference. Both algorithms were developed for special-purpose digital signal processors (DSPs). The CLSX algorithm uses the CSPI-based i860 DSP and the ARL-GORCA algorithm uses the Mercury-based SHARC DSP. These algorithms should be integrated into the UWBView software.

*Self-interference removal*.—This algorithm, developed by ARL, was also implemented using the Mercury-based i860 DSP. It should also be integrated in the UWBView software.

*Constant integration angle backprojection image former*.—The integrated image former algorithm mentioned in this report needs to be modified to keep the integration angle almost constant for all pixels in the image. ARL has been employing a stand-alone backprojection image former, which was implemented using Mercury-based i860s to produce constant integration angle imagery.

*Detection algorithms.*—Many stand-alone FOPEN and GPEN detection algorithms have been developed. They, too, should be integrated into this software environment.

# References


1. M. Ressler, L. Happ, L. Nguyen, T. Ton, and M. Bennett, *The Army Research Laboratory Ultra-Wideband Testbed Radars*, Record of the IEEE 1995 International Radar Conference, pp. 686–691.

2. Lam Nguyen, John McCorkle, and Jeffrey Sichina, *Interference Extraction Algorithm for Ultra Wideband Synthetic Aperture Radar*, U.S. Army Research Laboratory unpublished report, R-SRL-SE-RU-96-003 (December 1996).

3. T. Miller and J. McCorkle, "*Near Least Squares Radio Frequency Interference Suppression*, SPIE Radar Sensor Technology Conference Proceedings (April 1996).

4. J. McCorkle, and L. Nguyen, *Focusing of Dispersive Targets Using Synthetic Aperture Radar*, Army Research Laboratory, ARL-TR-305 (August 1994).

5. Lam Nguyen, Steve Choy, and Francois Koenig, *ARL's RailSAR and BoomSAR: Real-time Data Acquisition, Signal Processing, and Control System for Ultra-Wideband Synthetic Aperture Radar*, U.S. Army Research Laboratory unpublished report, R-SRL-SE-RU-96-002 (June 1996).

6. *TIFF Revision 6.0*, Aldus Corporation (June 1992).

7. Lam Nguyen, Ravinder Kapoor, Jeffrey Sichina, and David Wong, *Ultra-Wideband Radar Target Discrimination Utilizing an Advanced Feature Set,* Proceedings of SPIE, Algorithms for Synthetic Aperture Radar Imagery V (April 1998).

8. Lam Nguyen, Karl Kappra, David Wong, Ravinder Kapoor, and Jeffrey Sichina, *A Mine Field Detection Algorithm Utilizing Data from an Ultra-Wideband Wide-Area Surveillance Radar,* Proceedings of SPIE, Detection and Remediation Technologies for Mine and Minelike Targets III (April 1998).

9. Richard Rau and James McClellan, *Aspect Angle Information of Targets in UWB SAR Images and New Post Processing Techniques,* Proceedings of Advanced Sensors Consortium, ARL Federated Laboratory (February 1998).

10. Richard Rau, James H. McClellan, Worayot Lertniphonphun (Georgia Institute of Technology), Lam Nguyen, and Tuan Ton (U.S. Army Research Laboratory), *On The Design and Test of Advanced Two Dimensional Image Filters For Isolating Angle and Frequency Dependent Scattering Phenomena*, Proceedings of U.S. Army Research Laboratory Advanced Sensors Consortium (1999).

11. Richard Rau and James H. McClellan, *Postfiltering Techniques For Ultra-Wideband Wide Angle Synthetic Aperture Radar*, Proceedings of Army Research Laboratory Advanced Sensors Consortium (1999).

# Distribution

Admnstr
Defns Techl Info Ctr
Attn DTIC-OCP
8725 John J Kingman Rd Ste 0944
FT Belvoir VA 22060-6218

Ofc of the Secy of Defns
Attn ODDRE (R&AT)
The Pentagon
Washington DC 20301-3080

OSD
Attn OUSD(A&T)/ODDR&E(R) R J Trew
Washington DC 20301-7100

AMCOM MRDEC
Attn AMSMI-RD W C McCorkle
Redstone Arsenal AL 35898-5240

CECOM
Attn PM GPS COL S Young
FT Monmouth NJ 07703

Dir for MANPRINT
Ofc of the Deputy Chief of Staff for Prsnnl
Attn J Hiller
The Pentagon Rm 2C733
Washington DC 20301-0300

US Army Armament Rsrch Dev & Engrg Ctr
Attn AMSTA-AR-TD M Fisette
Bldg 1
Picatinny Arsenal NJ 07806-5000

US Army Edgewood RDEC
Attn SCBRD-TD G Resnick
Aberdeen Proving Ground MD 21010-5423

US Army Info Sys Engrg Cmnd
Attn ASQB-OTD F Jenia
FT Huachuca AZ 85613-5300

US Army Natick RDEC Acting Techl Dir
Attn SSCNC-T P Brandler
Natick MA 01760-5002

Director
US Army Rsrch Ofc
4300 S Miami Blvd
Research Triangle Park NC 27709

US Army Simulation, Train, & Instrmntn Cmnd
Attn J Stahl
12350 Research Parkway
Orlando FL 32826-3726

US Army Tank-Automtv Cmnd Rsrch, Dev, & Engrg Ctr
Attn AMSTA-TA J Chapin
Warren MI 48397-5000

US Army Train & Doctrine Cmnd
Battle Lab Integration & Techl Dirctrt
Attn ATCD-B J A Klevecz
FT Monroe VA 23651-5850

US Military Academy
Mathematical Sci Ctr of Excellence
Attn MDN-A MAJ M D Phillips
Dept of Mathematical Sci Thayer Hall
West Point NY 10996-1786

Nav Surface Warfare Ctr
Attn Code B07 J Pennella
17320 Dahlgren Rd Bldg 1470 Rm 1101
Dahlgren VA 22448-5100

DARPA
Attn B Kaspar
3701 N Fairfax Dr
Arlington VA 22203-1714

Hicks & Associates Inc
Attn G Singley III
1710 Goodrich Dr Ste 1300
McLean VA 22102

Palisades Inst for Rsrch Svc Inc
Attn E Carr
1745 Jefferson Davis Hwy Ste 500
Arlington VA 22202-3402

US Army Rsrch Lab
Attn AMSRL-DD J Rocchio
Attn AMSRL-CI-LL Techl Lib (3 copies)
Attn AMSRL-CS-AS Mail & Records Mgmt
Attn AMSRL-CS-EA-TP Techl Pub (3 copies)
Attn AMSRL-SE-RU B Merchant
Attn AMSRL-SE-RU B Scheiner
Attn AMSRL-SE-RU D Wong

## Distribution (cont'd)

US Army Rsrch Lab (cont'd)
Attn AMSRL-SE-RU G Smith
Attn AMSRL-SE-RU H Khatri
Attn AMSRL-SE-RU J Sichina
Attn AMSRL-SE-RU K Kappra
Attn AMSRL-SE-RU K Ranney
Attn AMSRL-SE-RU L Nguyen (10 copies)
Attn AMSRL-SE-RU M Conn
Attn AMSRL-SE-RU M Qaadri

US Army Rsrch Lab (cont'd)
Attn AMSRL-SE-RU M Ressler
Attn AMSRL-SE-RU R Damarla
Attn AMSRL-SE-RU R Kapoor
Attn AMSRL-SE-RU T Nguyen
Attn AMSRL-SE-RU T Ton
Attn AMSRL-SE-SR J Dammann
Attn AMSRL-SE-SS R Hansen
Adelphi MD 20783-1197

# REPORT DOCUMENTATION PAGE

*Form Approved*
*OMB No. 0704-0188*



| 1. AGENCY USE ONLY *(Leave blank)* | 2. REPORT DATE | 3. REPORT TYPE AND DATES COVERED |
|---|---|---|
| | September 1999 | Final, Sept 1997 to Sept 1998 |

**4. TITLE AND SUBTITLE** Visualization and Data Analysis Techniques for Ultra-Wideband Wide-Angle Synthetic Aperture Radar Data

**5. FUNDING NUMBERS**

DA PR: AH16
PE: 62120A

**6. AUTHOR(S)** Lam Nguyen

**7. PERFORMING ORGANIZATION NAME(S) AND ADDRESS(ES)**
U.S. Army Research Laboratory
Attn: AMSRL- SE-RU email: lnguyen@arl.mil
2800 Powder Mill Road
Adelphi, MD 20783-1197

**8. PERFORMING ORGANIZATION REPORT NUMBER**
ARL-TR-1959

**9. SPONSORING/MONITORING AGENCY NAME(S) AND ADDRESS(ES)**
U.S. Army Research Laboratory
2800 Powder Mill Road
Adelphi, MD 20783-1197

**10. SPONSORING/MONITORING AGENCY REPORT NUMBER**

**11. SUPPLEMENTARY NOTES**
ARL PR: 6NE4I2
AMS code: 622120.H16

**12a. DISTRIBUTION/AVAILABILITY STATEMENT** Approved for public release; distribution unlimited.

**12b. DISTRIBUTION CODE**

**13. ABSTRACT** *(Maximum 200 words)*

The U.S. Army Research Laboratory (ARL) has designed, developed, and constructed an ultra-wideband synthetic aperture (UWB SAR) imaging radar to detect obscured targets, such as vehicles concealed by foliage and objects buried underground. As part of this effort, ARL has developed the software called UWBView to support the study of this imaging radar. The software can be employed in both field test and laboratory situations. In a field test, it provides a tool to perform certain signal processing tasks and to quickly assess radar data quality. In the research environment, it provides analysts with data visualization and analysis capabilities to support the phenomenological studies of targets and clutter. In a data processing environment, the software performs data and signal processing tasks. This report discusses the current software features and sample studies of UWB radar data using the software.

**14. SUBJECT TERMS**
Ultra-wideband radar, SAR, foliage-penetrating radar, ground-penetrating radar, GUI, signal processing, focusing

**15. NUMBER OF PAGES**
52

**16. PRICE CODE**

| 17. SECURITY CLASSIFICATION OF REPORT | 18. SECURITY CLASSIFICATION OF THIS PAGE | 19. SECURITY CLASSIFICATION OF ABSTRACT | 20. LIMITATION OF ABSTRACT |
|---|---|---|---|
| Unclassified | Unclassified | Unclassified | UL |

NSN 7540-01-280-5500

Standard Form 298 (Rev. 2-89)
Prescribed by ANSI Std. Z39-18
298-102

DEPARTMENT OF THE ARMY
U.S. Army Research Laboratory
2800 Powder Mill Road
Adelphi, MD 20783-1197